Journal of Electronic Materials (2022) 51:2624–2644
https://doi.org/10.1007/s11664-022-09515-9

ORIGINAL RESEARCH ARTICLE

Electrical Resistivity and Magnetization Study on $LaFe_2As_2$, $La_{0.8}Ba_{0.2}Fe_2As_2$, and $La_{1-x}Ba_xPt_{0.1}Fe_{1.9}As_2$ ($x = 0$, 0.05, 0.2, 0.4, and 0.6) Superconducting Compounds

Cihat Boyraz[1] · **Yildirhan Oner**[2]

Received: 30 April 2021 / Accepted: 9 February 2022 / Published online: 8 March 2022

Abstract

We report the magnetic properties of $LaFe_2As_2$, $La_{0.8}Ba_{0.2}Fe_2As_2$, and $La_{1-x}Ba_xPt_{0.1}Fe_{1.9}As_2$ ($0 \le x \le 0.6$) compounds prepared by solid-state reaction in a wide temperature range of 5–300 K in a field up to 9 T. All as-prepared samples act as superconducting magnets at low temperatures under normal atmospheric pressure. The magnetic state of $LaFe_2As_2$ has been studied in detail in a temperature range of 5–200 K for the fields in between $H = \pm 1$ T. We conclude that the samples are made up of a large number of smaller and similar magnetic domains developed by the thermal agitation under the internal magnetic field during the cooling process. Considering $LaFe_2As_2$ as a parent compound, it is assumed that substituting of Ba^{2+} to the site La^{3+} results in hole doping similar to K doping in $Ba_{1-x}K_xFe_2As_2$. We have investigated the magnetic properties of $La_{1-x}Ba_x\ Pt_{0.1}Fe_{1.9}As_2$. The paramagnetic contribution to the magnetization is determined by fitting the M (H, 5 K) curve using the Langevin function for each sample. Then, from the paramagnetic subtracted M-H curves, the critical current density, J_c, and normalized pinning force $F_p/F_{p,\max}$ as a function of the applied field is obtained. Moreover, the normalized pinning force density, $F_p/F_{p,\max}$, curves versus $h = H/H_{irr}$ (H_{irr} is the irreversibility field) were scaled using the Dew–Hughes model. Hence, the nature of the flux-pinning centers is revealed. Based on the results obtained from these analyses, we claim that the superconductivity in all as-prepared samples occurs on the domain boundary with the filamentary character and bulk superconductivity inside the domains.

Keywords Iron-based superconductors (FeSC) · diamagnetism · magnetization · resistivity · critical current density · pinning forces in superconductors

Introduction

The discovery of superconductivity with critical temperatures up to 55 K in two families of layered iron arsenides[1–3] has led scientists to explore and discover new iron-based superconductors. These iron-based materials can be classified on the basis of their atomic structures using different codes for each, such as CuZrSiAs-type LnFeAsO (Ln1111) and $ThCr_2Si_2$-type $AeFe_2As_2$ (Ae122),[1,4–6] where Ln and Ae are lanthanoid and alkaline earth metal elements, respectively. The other structures are "111" Cu_2Sb-type LiFeAs,[7] "11" PbO-type FeSe,[8] "42622" Sr_2FeO_3CuS-type $Sr_4Sc_2O_6Fe_2P_2$,[9] and "10-3-8" phase $Ca_{10}(Pt_3As_8)(Fe_2As_2)_5$.[10,11] Among them, the 122 system has attracted the most interest because of similarities in their superconducting properties (SC) with those of the high-temperature superconducting cuprates (see the review paper of Stewart and Ref. 2 for further detail). Interestingly, the emergence of superconductivity in both families usually accompanies the suppression of a long-range antiferromagnetic (AFM) ordered state in a corresponding parent compound with both hole- and electron-doped or pressure. Such similarities might suggest a common origin for SC and, indeed, AFM spin fluctuations. The 122 system can be easily prepared by various techniques and open the way to investigate intrinsic physical properties and the close interplay between structure, magnetism, and superconductivity.[12]

✉ Yildirhan Oner
oner@itu.edu.tr

[1] Department of Mechanical Engineering, Marmara University, 34722 Istanbul, Turkey

[2] Department of Physics Engineering, Istanbul Technical University, 34469 Istanbul, Turkey

There are only a few papers published based on La-doped 122 systems[13–17] due to difficulties arising from samples synthesized by La. The $LaFe_2As_2$ compound can be considered an exceptional one among the other 122 systems due to electron doping level beyond 0.2e/Fe to destroy superconductivity observed for $AeFe_2As_2$-based superconductors (FeBS). However, very recently, Iyo et al.[18] found that when its crystal structure transforms from a collapsed tetragonal structure to an uncollapsed tetragonal structure by annealing, the sample becomes a superconductor at low temperatures (T_c = 12.1 K). Therefore, it is expected that the difference in the electronic structure of collapsed and uncollapsed $LaFe_2As_2$ may hold the key to understanding the origin of superconductivity, as discussed for other iron-based superconductors.[19,20]

This newly discovered compound has some properties that could lead to discussing the role of the valency of La atoms on superconductivity. The common idea is that electron doping beyond 0.2 e/Fe can break electron pairs and destroy the superconductivity in Fe-based materials (FeBS). Very recently, Mazin et al. argued[21] an unusual valance value of La in this compound and tried to clarify this puzzling behavior. They have found that the valence of Fe^{2+} is close to + 2.7, which corresponds to doping of 0.35e, rather than 0.5e; it is thus an acceptable level of overdoping. In fact, the heavily electron doping limit had already been exceeded for 1111-type Fe-based superconductors. For example, Hosono's group showed that it would be possible to go beyond the highest $Fe^{1.5+}$ valency on the 1111 material LaFeOAs, with up to 50% of O^{2-} replaced by H^-. Intriguingly, they observed two superconducting domes, possibly with different pairing symmetries and/or mechanisms[22–24]

As for the $LaFe_2As_2$ compound, one may consider it an end member of La-doped $BaFe_2As_2$, which can be obtained by the complete substitution of Ba^{2+} for La^{3+}, which corresponds to a very heavy electron doping of 50%. A band structure calculation of $LaFe_2As_2$ has shown that the hole FS around the Γ point is indeed missing due to the hybridization between La *d* and Fe *d* orbitals.[21] They have argued the role of the hopping mechanism between electron and hole bands (the direct hopping between La and Fe *d* orbitals and the indirect hopping through the As *p* orbitals) plays an important role in the spin fluctuation-mediated pairing scenario. Both studies indicate that the correspondence between the presence or absence of the hole FS and T_c can be naturally understood within the spin fluctuation-mediated pairing scenario.

On the other hand, the relationship between crystal structure and superconductivity in iron-based superconductors is often reported.[25–30] The tetrahedral geometry of the $FeAs_4$ significantly depends on the composition of the compounds and pressure. Governing T_c in FeSCs, the As−Fe−As bond angle of the FeAs tetrahedrons (αAs−Fe−As) and the As height from the Fe layers (hAs) are known important factors. The highest reported T_c value was obtained when the Fe–As–Fe angle reached the ideal value of 109.47° for a perfect tetrahedron. The deviation of the Fe–As–Fe bond angle from the ideal FeAs tetrahedron might be correlated with the density of states near the Fermi energy.[31]

They have pointed out that the disappearance of the d_{xy} hole FS or deeply moving below the Fermi level for the collapsed phase, as compared to that in the uncollapsed phase, is due to the large Fe–As–Fe bond angle (110.80° and 118.10° for uncollapsed and collapsed phases, respectively). They have also concluded that the hybridization between La *d* and Fe *d* orbitals originates from both the direct hopping between La and Fe *d* orbitals and the indirect hopping through the As *p* orbitals. That is, the nearest neighbor distance between La and Fe compared to that between Fe and As plays an important role in the hopping mechanism, which, in turn, imposes constraints on the spin fluctuation interaction.

In this paper, we study the interplay of spin fluctuations, and superconductivity in $LaFe_2As_2$ (La-122) compounds with La and Fe substituted by Ba (hole doping) and Pt (electron doping), respectively. We showed that hole doping leads to superconductivity, while, on the contrary, further electron doping suppresses the superconductivity, consistent with the band calculation predictions.

Experimental Procedure

Superconducting compounds were synthesized by combining highly pure equimolar (99.99%) La, As, Ba, Fe, and Pt, $LaFe_2As_2$ and $La_{1-x}Ba_xPt_{0.1}Fe_{1.9}As_2$ (x = 0, 0.05, 0.2, 0.4, and 0.6). All sample compositions were obtained in proper stoichiometries separately by solid-state reaction. At the first stage, depending on x steps, related chemicals were added into an agate mortar and mixed to form the desired stoichiometry.[15] The separately obtained samples were pressed by a rectangular-shaped pressing die. The pressed samples were then sealed off into quartz tubes and vacuumed. The samples were kept in a furnace for almost three days at 1150°C and released for self-cooling to room temperature. The sintered compositions in the quartz tubes were then taken from the furnace at room temperature and ground in an agate mortar separately. The samples were repressed for rectangular shapes and resealed into the quartz tubes to ensure the final desired compositions. The second sintering procedure, the same as the first, was applied to obtain a better homogeneity. To check the structural phase, standard θ–2θ measurements under operating details of 30 mA, 40 kV with Cu Kα source Rigaku SmartLab x-ray diffractometer (XRD) was used. The surface morphology of the $LaFe_2As_2$ sample was evaluated by scanning electron microscopy (SEM-EDX;

Jeol-6390-LV). Four-probe resistivity measurements were performed under a wide temperature range (5-300 K). The presented magnetic measurements were provided by a commercial physical property measurement system (PPMS; Quantum Design Model 6500) with an in situ attachment vibrating sample magnetometer (VSM).

Results and Discussion

Structural Analysis

The diffraction peaks of $LaFe_2As_2$, $LaPt_{0.1}Fe_{1.9}As_2$, and $Ba_{0.05}La_{0.95}Pt_{0.1}Fe_{1.9}As_2$ compositions synthesized by solid-state reaction are shown in Fig. 1. These samples revealed a $ThCr_2Si_2$-type body-centered tetragonal structure with a space group of I4/mmm. The ignorable unknown peaks were marked by an asterix (*) in $LaFe_2As_2$ and $La_{0.95}Ba_{0.05}Pt_{0.1}Fe_{1.9}As_2$ samples. The Debye–Scherrer method was used to calculate the crystallite size of all samples varying between 45 and 60 nm. Rietveld refinement (FullProf program) was used for indexing the patterns and calculating the lattice parameters of all compositions (see the other XRD patterns and lattice constants in our published paper[15]). As seen in Fig. 1a, Y_{obs}, Y_{cal}, Y_{obs}–Y_{cal}, and Bragg positions are the data taken from XRD, the data calculated by the FullProf program, the difference between Y_{obs} and Y_{cal}, and possible peak positions according to Bragg's law, respectively. The lattice parameters and cell volumes were calculated for the compositions $LaFe_2As_2$ ($a = 4.0034$ Å, and $c = 11.01445$ Å, and $V = 176.53$ Å^3), $LaPt_{0.1}Fe_{1.9}As_2$ ($a = 4.0036$ Å, and $c = 11.0145$ Å, and $V = 176.549$ Å^3), and $Ba_{0.05}La_{0.95}Pt_{0.1}Fe_{1.9}As_2$ ($a = 3.983$ Å, and $c = 12.995$ Å, and $V = 206.156$ Å^3). As seen in Fig. 1d, the SEM image of the $LaFe_2As_2$ sample is shown in a 10-μm area. Three different areas were chosen to figure out the elemental composition of each element. The atomic ratios of Fe, As, and La in the areas of spectrum 1, spectrum 2, and spectrum 3 are (Fe = 48.23, As = 38.85, and La = 12.92), (Fe = 40.54, As = 42.27, and La = 17.19), and (Fe = 46.41, As = 37.67, and La = 15.92), respectively. These results confirm that the desired stoichiometry of the $LaFe_2As_2$ main composition was achieved.

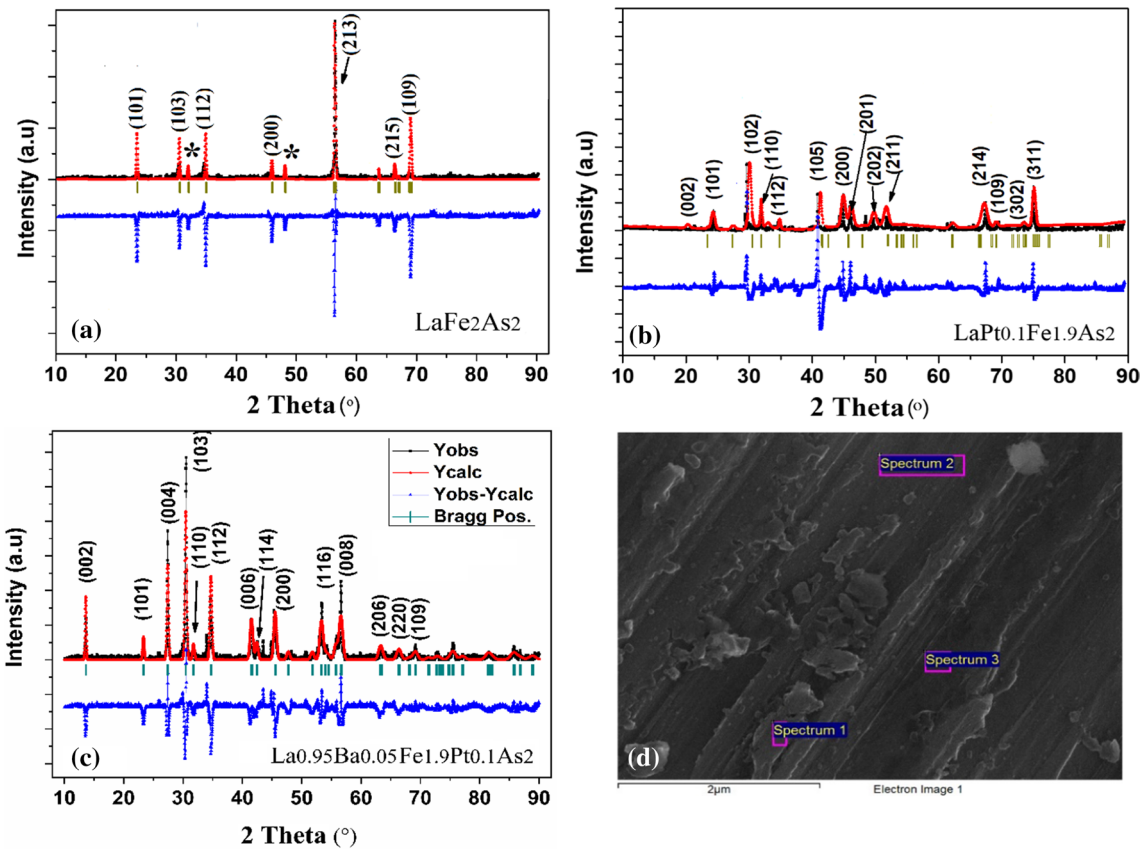

Fig. 1 XRD patterns and Rietveld refinements of $LaFe_2As_2$, $LaPt_{0.1}Fe_{1.9}As_2$, and $La_{0.95}Ba_{0.05}Pt_{0.1}Fe_{1.9}As_2$ in (a), (b), and (c), respectively. (d) SEM image of $LaFe_2As_2$.

Magnetic Analysis

Note that irreversibility still exists at our highest temperature, 400 K, pointing to a much higher temperature for T_{irr}. A small jump is observed on the M_{ZFC} (warming) curve at T_{cr} = 129 K and M_{FC} (cooling) at T_{cr} = 124 K curve. The insets on the right and left sides show the jumps on an expanded scale. The magnetization measurements were carried out on the sample of $LaFe_2As_2$ in the temperature range from 5 to 400 K at the applied magnetic field, H = 50 Oe. Magnetization data are taken in different cases: either during cooling in an applied field (FC) or while warming up after the sample has been cooled in zero field (ZFC). A large irreversibility in the zero-field-cooled versus field-cooled (ZFC/FC) magnetization is observed. The M_{ZFC} and M_{FC} branches of $M(T)$ curves separate at T = 400 K, our highest available temperature, as shown in Fig. 2.

In fact, $M(T)$ curves split into M_{ZFC} and M_{FC} branches at the irreversibility temperature, T_{irr}. It appears that the irreversibility occurs at a much higher temperature than T = 400 K. The observed magnetization (T) reveals some of the main features of a magnetic system consisting of a large number of magnetic entities (the assembly of particle systems). We see that the magnetization for both branches decreases with decreasing temperature until it falls to the critical temperature, T_{cr} where the sample exhibits a first-order structural transition. After the structural transition, M_{FC} changes its slope and increases with decreasing temperature, while M_{ZFC} continues to decrease. It is found that a structural first-order phase transition begins to occur at T_{cr} ~ 129 K in the ZFC case (during warming), while the transition takes place at T_{cr} ~ 124 K in the FC case (during cooling), as shown in the insets of Fig. 2 on the expanded scales. This behavior indicates a typical first-order structural transformation except that the peaks are not as intense as expected. It appears that the partial volume of the sample undergoes a first-order, structural phase transition to a low temperature (two phases coexist at low temperatures).

Figure 3 shows the field dependence of magnetization in the sample of $LaFe_2As_2$ at some selected temperatures such as at T = 5K, 20K, 50K, 150K, 200K, 300K, and 400 K in the field up to $H = \pm 1$ T. The M vs. H curves can be separated into two regions: one below and the other above T_{cr}. The M–H curves exhibit no hysteresis loop except at T = 5 K. Consequently, a hysteresis loop response is observed at T = 5 K (see the inset of Fig. 4a because the sample becomes a magnetic superconductor at lower temperatures.

As seen in Fig. 3, hysteresis is absent (except for M–H at T = 5 K with a little remanence and coercivity, H_c), which suggests the presence of a long-range magnetic dipole–dipole interaction among the assemblies of superparamagnetic nanoscale regions. Note that M–H curves split into two groups, one below 100 K, the other above 100 K. The hysteresis is likely to be associated with superconductivity, as described in the following paragraphs in detail. In this superparamagnetic state, the relative magnetization M/M_s can be described by the standard Langevin function, L, using the relation

$$M = M_s\left\{\coth\left[\mu_{\text{eff}}H/k_B(T + T_0)\right] - kB(T+T_0)/\mu_{\text{eff}}H\right\} + \chi H + M_0, \quad (1)$$

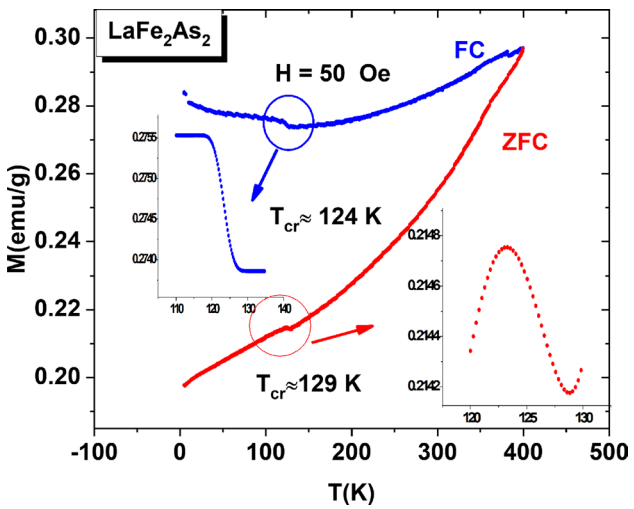

Fig. 2 Temperature dependence of magnetization for $LaFe_2As_2$ at H = 50 Oe in the zero-field case (M_{ZFC}) and the field-cooled case (M_{FC}).

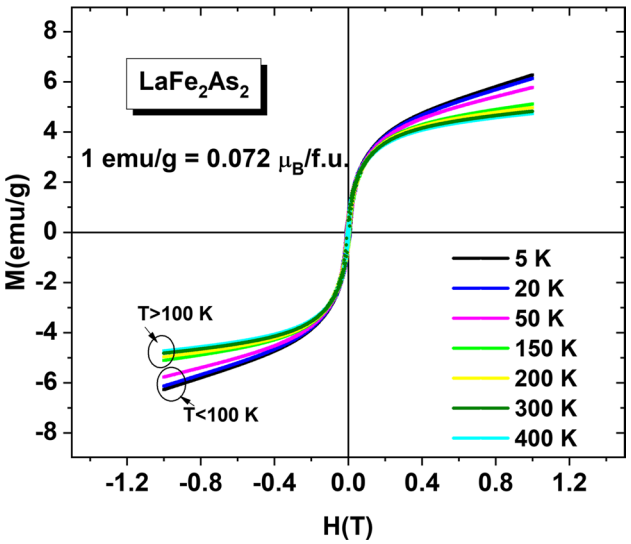

Fig. 3 The magnetization vs. field plots (M vs. H hysteresis loops) at selected temperatures for $LaFe_2As_2$.

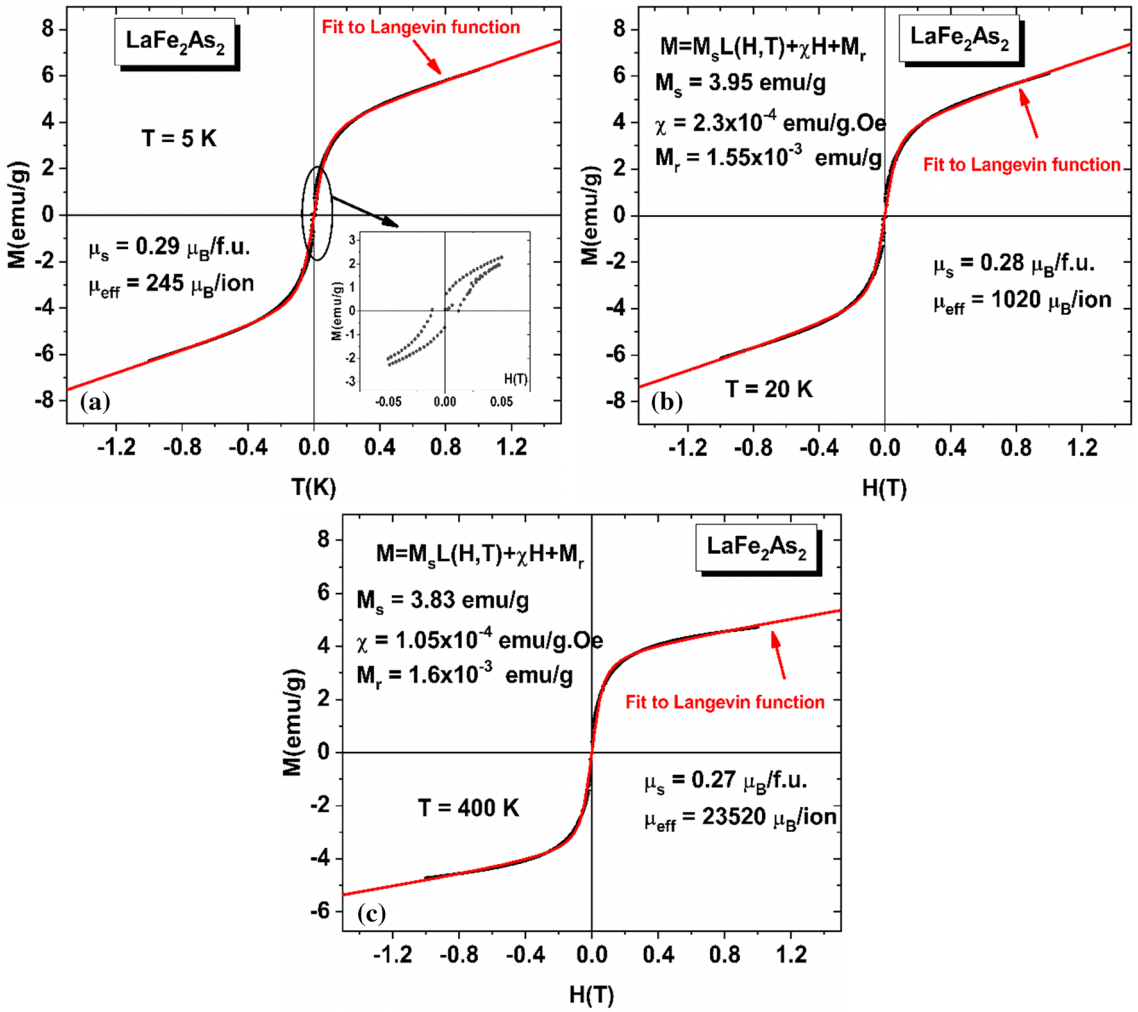

Fig. 4 M_{rev} versus H together with Langevin fit (a) at $T = 5$ K. The continuous red line shows M_{rev} vs. H together with the data fit to Langevin function. Inset displays the magnetization data at low fields with a weak hysteresis on an expanded scale. (b) $T = 20$ K. There is no hysteresis. M is completely reversible. The red line gives the fitting curve by using the Langevin equation. (c) $T = 400$ K. It demonstrates the Langevin fit quality at higher temperatures.

where M_s is the saturation magnetization value for assembly of a cluster and μ_{eff} is the magnetic moment for each cluster, T_0 is the effective Curie–Weiss temperature for the superparamagnetic clusters. The second term denotes the contributions from the paramagnetic impurity ions. This contribution might be emerging from some defects, as described above. The fitting of the magnetization data to the above Langevin function for $T = 5$ K, $T = 20$ K, and $T = 400$ K has been demonstrated in Fig. 4a, b, and c, respectively.

The fitting parameters M_s, μ_{eff}, χ, and M_0 are estimated from the best fitting and shown in Fig. 4 a, b, and c. T_0 is found to be less than 1 K for all temperatures, suggesting a weakly antiferromagnetic-like intercluster interaction. It should be noted that μ_s stays almost constant, slightly decreasing with the increasing temperature. The other fitting parameters obtained from the best fitting to the above Eq. 1 are summarized in Fig. 5.

Note that the magnetic susceptibility χ at higher temperatures obeys with a reasonable accuracy this modified Curie-Weiss law (Eq. 4 in the text). The upper inset gives the temperature dependence of μ_{eff}, as a plot using a logarithmic scale for both the μ_{eff}-axis and the T-axis. It is worth noting that μ_{eff} in terms of μ_B per cluster increases linearly with the temperature by 52 μ_B/K ion. The lower inset on the left shows the magnetic moment that originated at the As vacancy, μ_{As} normalized to its maximum value, $\mu_{\text{As,max}}$ (= 13.5 μ_B/As vacancy as indicated in the figure) as a function of the temperature. Note that the paramagnetic moments have been extracted from the modified Curie law. The lower inset on the right indicates $d\chi/dT$ versus T, and the curve passes through a minimum at 55 K, as indicated

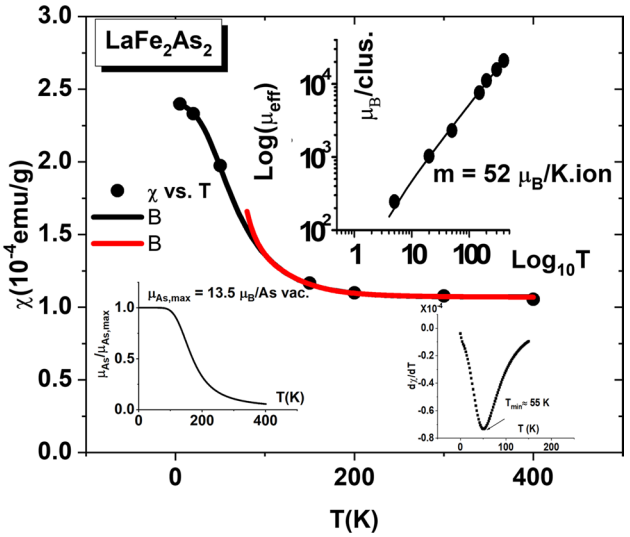

Fig. 5 Paramagnetic susceptibility χ versus T is plotted for the $LaFe_2As_2$. The red line is the fit to Eq. 4, as described in the text.

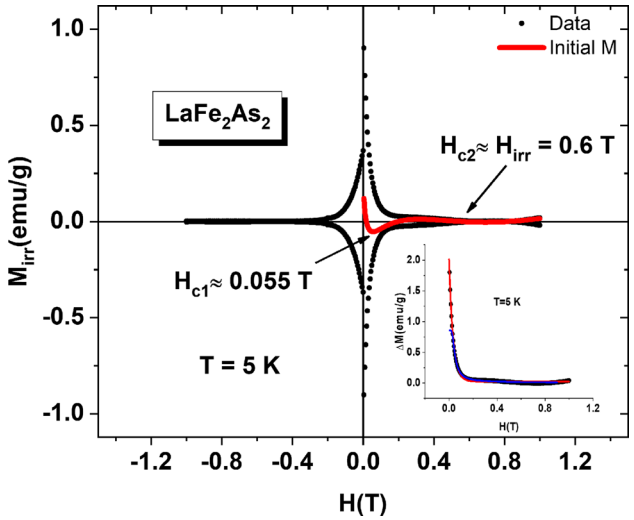

Fig. 6 M_{irr} versus H at $T = 5$ K for the $LaFe_2As_2$ after subtracting the paramagnetic contribution from M measured as described in the text.

in the figure. The paramagnetic impurity susceptibility χ is plotted as a function of the temperature in the range of 5–400 K, which shows a typical paramagnetic behavior. The data below T_{cr} pertaining to the high-temperature phase can be well described by the standard modified Curie–Weiss equation for the presence of the temperature variable magnetic impurity moment.[32] We use the following expression for the susceptibility:

$$\chi = C/([1 + n\mathrm{Exp}(-E_{exc}/(kBT))](T + TN)) + \chi_0 \text{ and } C = N(<\mu_{eff}^2>)/(3kB), \quad (2)$$

where N is the Avogadro number, $n = N_1/N_2$; N_1 is the number of the site with $<\mu_1^2>$ magnetic moment, N_2 is the number of the site with $<\mu_2^2> \approx 0$. $E_{exc} = E_2 - E_1$, where the energies of these two states are E_1 and E_2. The E_{exc} energy can be regarded as the energy required to form a local moment of $<\mu_1>$ on iron sites in the lattice. The best-fitting values are $C = 0.0566$ emu K/g Oe ($\mu_{eff} \sim 13.5$ μ_B/cluster), $T_N = -56$ K (tendency to become ferromagnetic), $n = 137$, $E_{exc} = 835$ K, and $\chi_0 \sim 1 \times 10^{-4}$ emu/g Oe. The susceptibility, χ presents the total paramagnetic moment arising from the impurities, defects, or other sources. Grinenko et al.,[33] pointed out that a disorder in the As-deficient sample of $LaFeAs_{1-\delta}O_{0.9}F_{0.1}$ superconductors gives rise to the formation of an electronically localized state around each As vacancy (AV) carrying a magnetic moment of about 3.2 μ_B per AV or 0.8 μ_B/Fe atom. Since the As vacancies in the La-1111 compound behave as magnetic defects with a net magnetic moment associated within [$VAsFe_4$], they observed a strong enhancement of the spin susceptibility by a factor of 3–7. We also assume that the As vacancies in the $LaFe_2As_2$ compound give rise to the formation of some paramagnetic spin clusters of unknown origin. Based on this study, the main contribution to the magnetization in $LaFe_2As_2$ has been attributed to the As vacancies. Under this condition, the As vacancies of paramagnetic contribution, normalized to its maximum value as a function of the temperature, are plotted in the lower inset of Fig. 5. The other lower inset depicts the temperature derivative of the susceptibility, passing through a minimum at about 55 K. It is likely that a partially magnetic phase transition occurs at around this temperature.

In the study of the coexistence of superconductivity, we know from our studies[15–17] and previous reports that M versus H decomposes into two parts, namely, $M = M_{rev} + M_{irr}$.[34,35] The magnetization which has a field-dependent positive contribution to the magnetization (M_{para}, hereinafter referred to M_{rev}) superimposed on the diamagnetic response originated from superconductivity. According to the Bean model,[35] the arithmetic mean value of the upper (M_+) and lower (M_-) branches of hysteresis, ($(M_+ + M_-)/2$) gives the reversible component, while the irreversible component is associated with superconductivity, assuming that the ferromagnetic hysteresis arising from the lattice or ferromagnetic impurities is negligible if it exists. The critical current density is related to the hysteresis cycle width, $\Delta M = |(M_+ - M_-)|$ by the equation $J_c = (15|\Delta M|)/R$ where R is the radius of the sample in cm, J in A/cm^2, and M in emu/cm^3. Following the same procedures used in our previous works for similar Fe-based superconductors, the M_{irr} versus H curve for $T = 5$ K is obtained after subtracting the paramagnetic contribution

from the measured *M–H* loop as described above and plotted in Fig. 6.

In Fig. 6, the arrows indicate the H_{c1} and $H_{c2} \approx H_{irr}$, respectively. The lower inset displays ΔM versus H, where ΔM is obtained from the upper and lower branches of the M vs. H hysteresis curve as to be $\Delta M = \frac{1}{2}(M_+ - M_-)$. The continuous blue line gives the fit to Eq. 4, as described in the text. It is noted that we obtain a typical superconducting magnetization hysteresis curve. The first critical field H_{c1} and the second critical field H_{c2} (here, H_{irr} is taken approximately to be H_{c2}) values are determined to be 0.055 T and 0.5 T, respectively. Here, we claim that $LaFe_2As_2$ is a superconducting ferromagnet (The magnetic irreversibility occurs at temperatures higher than the onset temperature of superconductivity, $T_{irr} > T_{sc}$), whereas Iyo et al. recently pointed out[18] that the observed superconductivity in the collapsed La122 sample (the sample as prepared) is due to a small amount of uncollapsed La122 component included in the sample. We believe that, in order to clarify this assertion, the magnetoresistance measurements would be a highly useful microscopic probe to reveal the existence of some local (its size is larger than the mean free path of the conduction electrons) superconductivity in the magnetic or non-magnetic matrix.[36]

We have also calculated ΔM as a function of the field H and plotted as shown in the inset of Fig. 6 Using the above equation for J_c, we obtain the critical current density to be $J_c(0) \sim 2 \times 10^4$ A/cm^2 at zero field for $T = 5$ K. It is shown that ΔM (αJ_c) decays exponentially with the applied field. The best fit the data to the equation, $\Delta M = \Delta M_0 + A\exp(-H/H_0)$ yields the fitting parameters, $\Delta M_0 = 0.02$ emu/g, $A = 2$ emu/g, and $H_0 = 0.0335$ T. On the other hand, in our previous study,[15] the ratio of $J_c(H)/J_c(0)$ can be expressed in terms of the activation energy, U, and some fitting parameters k_1 and k_2 related to the vortices pinning nature. Using the Poisson distribution of the vortices, one can obtain the following formula (see Eq. 4 in Ref.[15]):

$$J_c = J_c(0)/\left[1 + k_1 \exp(-1/x) \cdot x^{\alpha}\right] \quad \text{with } x = H/k_2 \qquad (3)$$

The data are fitted to Eq. (3), and the best-fitted parameters are $k_1 = 2.45$, $k_2 = 0.155$ T, $\alpha = 0.44$, and $J_c(0) = 1.2 \times 10^4$ A/cm^2. It should be noted that the data near $H = 0$ deviates from the fitting curve. These data may be attributed to the surface effect. Indeed, these data are not symmetric with respect to the field direction owing to the avalanche of the flux jumps [15 and references therein].

It is also possible to explore the field dependence of the pinning force. The pinning force density depends on the pinning of the flux distribution in the fluxoid lattice against Lorentz-like electromagnetic forces ($F = \gamma/cJxB \approx JB/c$, in sufficiently high fields $\gamma \approx 1$). Magnetization relaxation in superconductors occurs because of the nonequilibrium spatial distribution of vortices. The critical equilibrium state is determined by the competition of the Lorentz force, the disorder-induced pinning force, and the thermal fluctuation. The critical current is defined when the Lorentz force is just balanced by the pinning force. In the critical state, the interaction between the vortices and all microstructural defects gives rise to a pinning force F_p. The normalized pinning force $f = F_p/F_{p,max}$ as a function of reduced field $h = H/H_{c2}$ (here it is considered to be $H_{c2} \approx H_{irr}$) is found to obey a scaling relation, i.e., $f = Ah^p(1-h)^q$ in which A is a prefactor, p and q are the exponents that describe the actual pinning mechanism.[15] The normalized pinning force $f = F_p/F_{p,max}$ based on the model of Dew–Hughes can be modified to account for flux creep effects as follows[37–40]:

$$f = A_0 h^p (1-h)^q [1 + \mu\beta|S|]^{-1/\mu} + f_0 \qquad (4)$$

where S is the static flux rate, the exponent μ is an important parameter to characterize both the relaxation and vortex dynamics. The activation energy, U can be related to β with the relation by $U(J_c, H) = k_B T\beta$ (here, $\beta = ln\,(t_m/\tau_o)$, t_m is the measurement time, τ_o is the characteristic relaxation time for reaching from the initial non-equilibrium state to the equilibrium state, as is intrinsic to the system). The term f_0 is the background field-independent part. Figure 7 shows f versus h curves for the sample, $LaFe_2As_2$. The curve consists of two successive peaks, with the first narrow and intense peak at $h \approx 0.06$ and the second magnetization peak (SMP) at $h \approx 0.6$, much broader, which is associated with a crossover from elastic to plastic vortex creep. In higher fields, the critical current density is affected by flux creep, whereas, in the low field regime, the grain boundaries appear to pin the

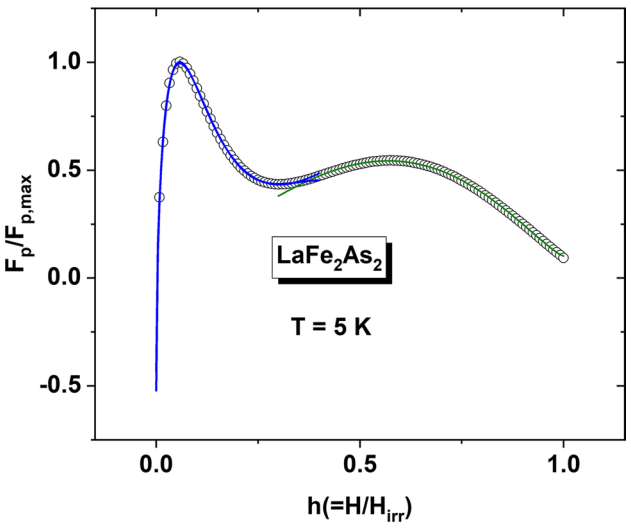

Fig. 7 The normalized pinning force density, $F_p/F_{p,max}$, curves versus $h = H/H_{irr}$ (H_{irr} is the irreversibility field) at $T = 5$ K is plotted sample of $LaFe_2As_2$.

flux lines. At the low field, the supercurrent does not flow homogeneously and strongly depends on usually randomly oriented grains.[41] The pinning on the grain boundary produces a low field maximum in the field dependence of pinning force density. But a collective creep pinning becomes progressively easier with increasing field and the second maximum in F_{pin} has been attributed to the effect of collective pinning of vortices. Above the crossover, plastic vortex creep governs the vortex. Since $S \propto (J_c/J_{c0})^{\mu}$,[42–45] for the fitting to the lower field, we assume $S = S_0\exp(-\alpha h)h^n$. It should be noted that J_c decays exponentially at lower fields. By inserting this term into Eq. 4, we get $f = A_0h^p(1-h)^q[1+\mu\beta S_0\exp(-\alpha h)h^n]^{-1/\mu} + f_0$. The best fitting parameter values are $A_0 = 7.26$, $p = 0.46$, $q = 0.97$, $\mu = 1/7$, $\alpha = 6.4$, $n = 1.86$, $\mu\beta S_0 = 11.1$, and $f_0 = -0.43$ for the first peak. As for the SMP, we assume $S \propto h^n$ and insert $S = S_0 h^n$ term. The best fit to the SMP yields the fitting parameters $A_0 = 4.63$, $p = 2$, $q = 1$, $\mu = 1/7$, $n = 2$, $\mu\beta S_0 = 0.157$, and $f_0 = 0.09$.

Note that $F_p/F_{p,max}$ exhibits two separate second magnetization (SM) peaks. Data were scaled using the Dew–Hughes model. The continuous line indicates the fits with different colors with SM peaks using Eq. 5, as described in the text.

According to the obtained fitting parameters, the results can be interpreted as follows: (1) there are two kinds of pinning centers. At low fields, the normal surface pinning becomes dominant (perhaps, on the grain boundaries) while, at high fields, the results indicate Δk-pinning, point pins (inside the grains). (2) The field dependence of S in the range of $0 < h < 1$ can be obtained by combining the low fields and high fields results in a single S curve, normalized to its value at $H = H_{irr}$ (see Fig. 8). As a result, we conclude that the as-prepared $LaFe_2As_2$ sample consists of a number of smaller and similar magnetic domains (or clusters) developed by thermal agitation and magnetic field and becomes a superconductor at about $T \sim 14$ K (see also the resistivity, Fig. 19a) such that the filamentary (between domain boundaries) and bulk (inside the domains) superconductivity coexist.

Pt has a strong spin-orbit coupling (SOC) due to 5d electronic orbitals. It is well known that strong spin-orbit coupling and its strong correlations in electronic structure lead to a number of exotic physical phenomena in the system. We believe that, doping Pt in $LaFe_2As_2$, might cause a great influence by the SOC on the electronic degrees of freedom of the system, which, in turn, plays an important role in the participation of both in the magnetic and in the superconducting properties.

Figure 9 shows the temperature dependence of M_{ZFC} versus M_{FC} at $H = 20$ Oe for the sample of $LaP_{0.1}Fe_{1.9}As_2$. The irreversibility shifts significantly toward low temperature upon Pt doping when compared to that of $LaFe_2As_2$ and occurs below 250 K. Above T_{irr}, M_{ZFC}, and M_{FC} merges, the magnetization increment linearly with temperature, T. Above T_{irr}, the susceptibility, χ is given by $\chi(T) = \chi_0 (1 + aT)$ at $H = 0.02$ T in which $\chi_0 = 8.15 \times 10^{-5}$ emu/g Oe (~ 3.37×10^{-2} emu/mol) and $a = 5.37 \times 10^{-3}$ K^{-1}.

Note that M_{FC} changes its slope and turns up at $T_{cr} \approx 126$ K. As the temperature further drops, it is leveling off. It is also worth noting that M increases linearly with T (universal linear temperature behavior of the susceptibility) above T_{irr}. The inset on the left shows dM_{ZFC}/dT versus T, and the arrow indicates T_m where the curve passes through a maximum ($T_m = 93$ K). The inset on the right displays M_{FC} versus T under $H = 2$ Oe cooling field. The arrows indicate the

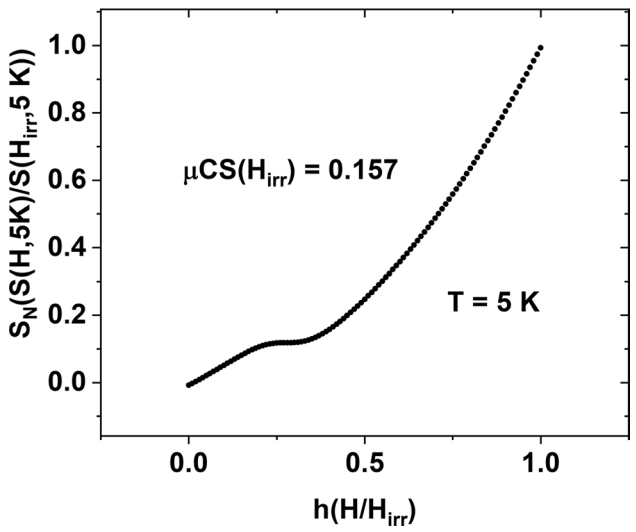

Fig. 8 The field dependence of relaxation rate, $S(H, T)$ normalized to its value at $H = H_{irr}$ in the range of $0 < h < 1$ at $T = 5$ K, where $h = H/H_{irr}$.

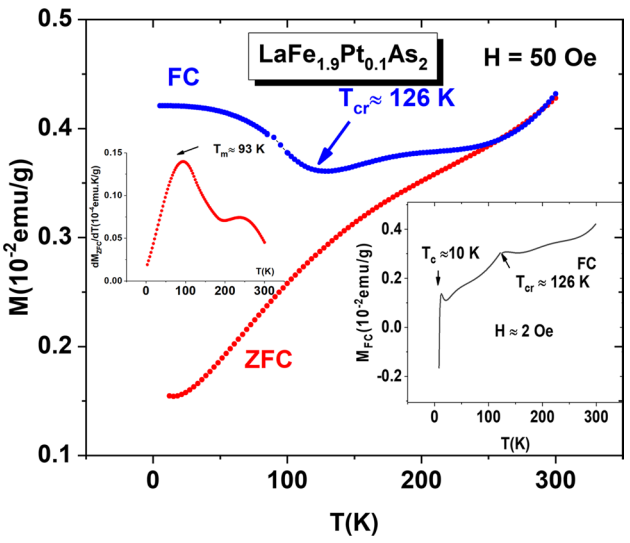

Fig. 9 $M_{ZFC}(T)$ versus $M_{FC}(T)$ at $H = 50$ Oe for $LaPt_{0.1}Fe_{1.9}As_2$. Note that $M(T)$ splits into two branches (referred to as M_{ZFC} and M_{FC}) at $T_{irr} \sim 250$ K.

critical temperature, $T_{cr,}$ and superconducting phase transition temperature, $T_c \approx 10$ K.

Thus, the universal linear temperature dependence susceptibility suggested for Fe-HTCS is confirmed, but it is held at high fields.[46] M_{FC} increases suddenly at $T_{cr} \approx 126$ K (and then levels off at lower temperatures), which is very close to the structural transition temperature, T_{cr} inferred from the sharp drop in M_{FC} and M_{ZFC} curves for $LaFe_2As_2$ (see Fig. 2). M_{ZFC} curve decreases gradually with decreasing temperature; no superconductivity is observed in our temperature measurement range. However, when the sample is cooled under a very low field (in our experiment, the applied field is estimated to be less than $H = 2$ Oe), it becomes 100% bulk superconducting at around $T = 10$ K (see the inset of Fig. 9). The existence of superconductivity is evidenced from a sharp drop in the FC data in $H = 2$ Oe at $T = 10$ K (The value of $4\pi\chi$ (FC) at 5 K exceeds -1, indicating that the shielding volume fraction at 5 K is almost 100%, a full Meissner state) and, in particular, from the zero resistance at this temperature in the resistivity measurement as given below. The other most remarkable finding concerned the large diamagnetic observed in the magnetization below T_{cr}. Similar behavior has already been observed in some other Fe-based superconductors [32 and references therein]; its origin is still under consideration. Figure 10a presents M_{ZFC} versus M_{FC} at $H = 20$ Oe in the temperature range of 5–150 K for $La_{0.95}Ba_{0.05}Pt_{0.1}Fe_{1.9}As_2$ in the three different modes. The sample was first cooled from the room temperature down to 5 K in the applied field, H ~ −0.5 Oe. Subsequently, the magnetic field of 20 Oe was then applied. The magnetization $M_{ZFC}(T)$ was obtained while the sample was slowly warmed up to 300 K. As for the field-cooled magnetization, $M_{FC}(T)$ measurements, the sample was cooled down again to 5 K without turning the magnetic field off. The most remarkable observed features are concerned with a sharp drop in the initial magnetization at T ~ 100 K and giant diamagnetism below 90 K. This diamagnetic signal stabilizes and decreases gradually but slightly until T_{sc} ~ 17.5 K, where the superconducting phase transition occurs. The curve changes the slope and goes up with $\Delta M_{sc} \sim 3 \times 10^{-3}$ emu/g down to 5 K.

In Fig. 10, the arrows indicate the initial measurement and subsequent measurement of magnetization. Initially, the sample is cooled down from room temperature to 5 K in the field of $H \sim -0.5$ Oe and then $H = 20$ Oe is applied. Note that the initial curve is upturned slightly at $T \sim 17.5$ K, 21.5

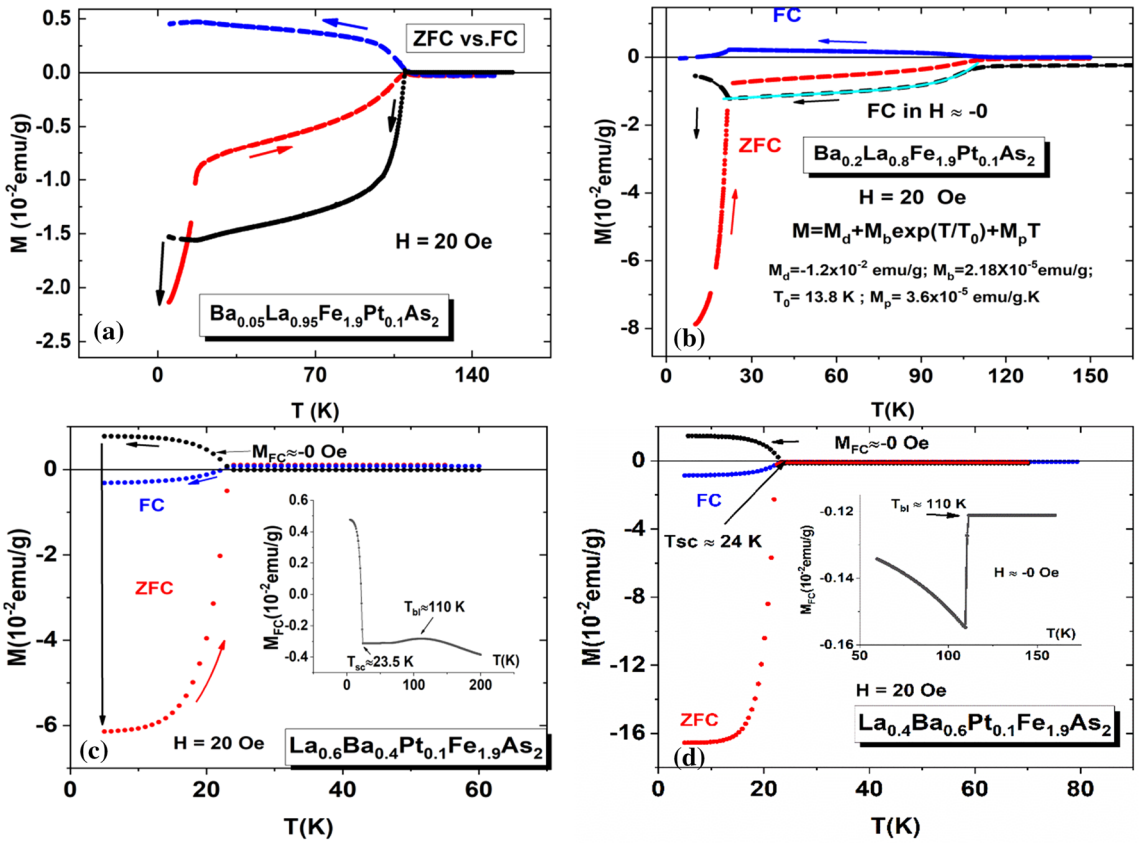

Fig. 10 Temperature dependence of magnetization, *M(T)* for (a) for $La_{0.95}Ba_{0.05}Pt_{0.1}Fe_{1.9}As_2$, (b) for $La_{0.8}Ba_{0.2}Pt_{0.1}Fe_{1.9}As_2$, (c) for $La_{0.6}Ba_{0.4}Pt_{0.1}Fe_{1.9}As_2$, (d) for $La_{0.4}Ba_{0.6}Pt_{0.1}Fe_{1.9}As_2$.

K, 23.5 K, and 24 K with increasing Ba content due to bulk superconductivity. The insets of Fig. 10c and d present the magnetization data plotted on an expanded scale to demonstrate the sample when cooled down in a very small field, whether positive or negative, a negative magnetization is produced, and thus the susceptibility becomes negative. It is noticed that the total detected diamagnetic moment between 90 and 110 K, $\Delta M_D \sim -1 \times 10^{-2}$emu/g at $H \sim -0.5$ Oe. It should be noted that, unless the external field, *H,* exceeds the demagnetization field $H_D = 4\pi M(H_D)$, the diamagnetic signal does not change its polarity, implying that the sample is cooled down in the internal field of the sample H_{int}. At $T \sim 17.5$ K, the system undergoes a superconducting phase transition in the field of $H = 20$ Oe. The shielding volume fraction at 5 K (bulk superconductivity) is estimated to be $\eta \sim 10\%$ at $H = 20$ Oe. Here, we should emphasize that Ba doping (even a very small amount of doping, 0.05% Ba) results in a drastic change in the superconducting properties of $LaPt_{0.1}Fe_{1.9}As_2$.

Figure 10b shows M_{ZFC} versus M_{FC} as a function of the temperature in the range of 5-150 K at $H = 20$ Oe for the sample of $La_{0.8}Ba_{0.2}Pt_{0.1}Fe_{1.9}As_2$. This sample has quite similar behavior to that observed in the previous sample. The only difference between these samples arises from the values of superconducting parameters, such as $T_{sc}$and the superconducting volume fraction, induced by Ba doping. We find $T_{sc} \sim 21.2$ K, $\eta \sim 40\%$, and almost the same $\Delta M_D \sim -1 \times 10^{-2}$ emu/g at $H \sim -0.5$ Oe for this sample. In our previous work,[32] we observed a similar giant diamagnetism in the $BaFePtAs_2$ compound. We point out here that the micro- (or nano-) scale ferromagnetic domain formations in the demagnetized state play a similar effect on the magnetic state in the case of the coexistence of magnetism and superconductivity. In the sample below 110 K, in order to demonstrate the formation of the magnetic ordering on nanoscale with a diamagnetic contribution, we assume that magnetization has two kinds of components; one is a pure diamagnetic contribution, the other is a paramagnetic component, which varies linearly with temperature. Here, the exponential term reflects from thermal agitation of the ordered magnetic regions (domains frozen with decreasing temperature). We use the formula $M = M_d + M_b\exp(T/T_0) + M_pT$, for the fitting of *M* data taken under a very small external field. We get a perfect fit with the best fitting parameters' values: $M_d = -1.2 \times 10^{-2}$ emu/g, $M_b = 2.18 \times 10^{-5}$emu/g with $T_0 = 13.8$ K and $M_p = 3.6 \times 10^{-5}$ emu/g K. When compared with those obtained parameters in our previous work, along with this respect for $BaFePtAs_2$, it seems that all these results are quite reasonable. Similar measurements have been carried out for the other compounds, $La_{0.6}Ba_{0.4}Pt_{0.1}Fe_{1.9}As_2$ and $La_{0.4}Ba_{0.6}Pt_{0.1}Fe_{1.9}As_2$, as shown in Fig. 10c and d, respectively. We find $T_{sc} \sim 23.2$ K, $\eta \sim 35\%$ for the former sample and $T_{sc} \sim 24$ K, $\eta = 100\%$ (The value of $4\pi\chi$ (ZFC) at 5 K exceeds -1, indicating that the shielding volume fraction is 100%) for the later, at $H = 20$ Oe in both samples. Close inspection of the data at higher temperature reveals that the diamagnetic contribution still exists in both samples (see the insets Fig. 10c and d, for each sample), but the signal is reduced by a factor of 10 for the former sample. Interestingly, it remains on the same order for the latter as compared to those observed for the first two samples. It should be noted that this diamagnetic signal manifests as a jump in the magnetization, as shown on an expanded scale version of Fig. 10d at higher temperatures (see the inset of Fig. 10d.

We have also measured *M(H)* for the samples of $La_{1-x}Ba_xPt_{0.1}Fe_{1.9}As_2$ ($x = 0.05$; $x = 0.2$; $x = 0.4$ and 0.6) at 5 K in the field range 0–9 T (Fig. 11). As long as Ba content increases, the superconducting irreversibility in the isothermal magnetization gradually gets weakened such that *M(H)* approach towards typical modeling superparamagnetic (SPM) behavior. To investigate the origin of exclusion irreversibility with decreasing Ba doping, in our first attempts, the magnetic isotherms were analyzed by considering the fact that there are two main types of elementary mechanisms changing the magnetization, reversible and irreversible. The irreversible processes are responsible for magnetic and thermomagnetic hysteresis as well as time-dependent magnetization phenomena (including the contribution of superconductivity to the irreversibility effects). In order to explore SC, the reversible part of the magnetization $M_{rev} = (M_+ + M_-)/2$ where and M_+ and M^- are upper and lower branches of the *M* vs. *H* curves) was subtracted from the *M(H)* curves. We can decompose *M* versus *H* into two parts, namely, $M = M_{rev} + M_{irr}$, as mentioned above. M_{rev} versus *H* is plotted in Fig. 12.

M_{irr} versus *H* is also presented in Fig. 13a, b, c, and d for each sample separately. The shape of *M(H)* for $x = 0.05$

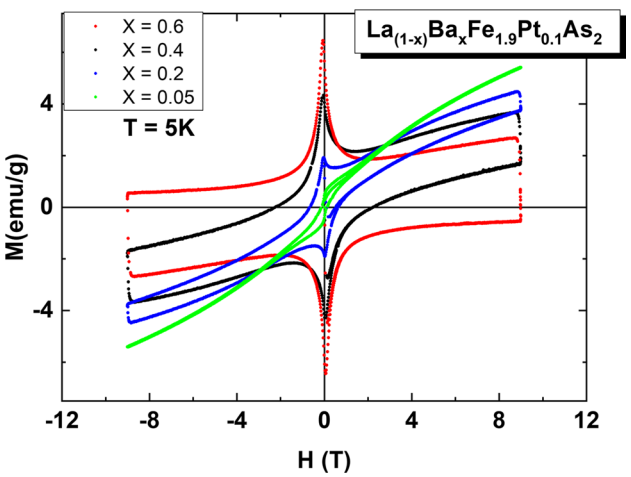

Fig. 11 Field dependence of magnetization at 5 K for the $La_{1-x}Ba_xPt_{0.1}Fe_{1.9}As_2$ ($x = 0.05$, 0.2, 0.4, and 0.6) compounds. Note that all the samples exhibit the Meissner Effect. The paramagnetic contribution increases with increasing Ba content.

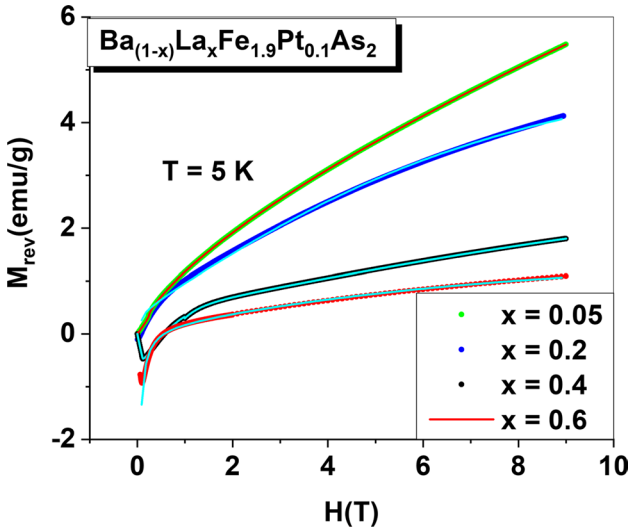

Fig. 12 M_{rev} versus H (up to 9 T) at T = 5 K for the $La_{1-x}Ba_xPt_{0.1}Fe_{1.9}As_2$ (x = 0.05, 0.2, 0.4, and 0.6) compounds. Note that the fitting curves using the Langevin expression are presented for all the samples with continuous lines of the same color (cyan) .

suggests that we should consider the presence of an SPM phase in this compound. This *S*-shaped hysteretic *M(H)* curve for $x = 0.05$ could have its origin in short-range ferromagnetic ordering or a superparamagnetic (SPM)-like state or a combination of both. Note that the continuous red lines give the initial magnetization curves. Figure 13d presents M_{irr} versus H at 5 K up to the ± 2 T field to see low-field details for $x = 0.6$. Figure 13e shows M versus H for positive H field-side up to $H = 9$ T. It is exclusively plotted to see high-field behavior. Note that M, ΔM, and M_{rev} are presented in the same figure in comparison with each other for $x = 0.6$. Indeed, we obtained reasonably a good fit for all the *M(H)* curves, by considering the equation $M(H) = M_{Ls}(x) + M_0$ where $x = \mu_{eff}H/k_BT$. M_s represents the saturation magnetization, μ_{eff} is the average magnetic moment per ion, $L(x) = \coth(x) - 1/x$ is the Langevin function, and M_0 is the temperature-independent term as mentioned above. The results of these fits are listed in Table I.

It can be seen from the table that for all samples the effective magnetic moments are close to each other and lie between $\mu_{eff} = 1.8 - 2.3\ \mu_B$/ion, whereas the saturation magnetization, μ_s decreases linearly with temperature as Ba doping increases. The saturation magnetization increases linearly with decreasing Ba content, x, which can be well described by the straight-line equation of $M_s = 8.85 - 12.6x$ (emu/g) (x is the atomic percent of Ba doping).

This result indicates that the magnetic ordering correlation length decreases with increasing Ba atoms, but the bulk superconducting volume fraction increases with Ba, as mentioned above. This behavior leads us to suggest that the magnetic order competes with the superconducting ground state in this system. On the other hand, as already discussed above, the critical current density, $J_c(H, T)$, is proportional to the $\Delta M = (M_+ - M_-)$. We have also calculated J_c as a function of the field, H at $T = 5$ K for all samples, and $J_c(H)$ normalized to their zero-field values $J_c(0)$ at $T = 5$ K is plotted as shown in Fig. 14. The critical current density, J_c ($T = 5$ K; $H = 0$ Oe) of the sample of $La_{0.4}Ba_{0.6}Pt_{0.1}Fe_{1.9}As_2$ is thus estimated to be ~ 1.8×10^5 A/cm^2. $J_c(0)$ versus x, Ba content. The current density, $J_c(0)$ at $T = 5$ K, showed a linear behavior with the x content (see the inset of Fig. 14). The most remarkable feature in these figures is that J_c drops exponentially with temperature as

$$J_c(T)/J_c(0) = a - \exp\left(-H/H_0\right) + j_0 \quad (5)$$

where H_0 is an empirical characteristic field value. The fit using Eq. 5 yields the fitting parameters H_0 for each sample. The results are summarized in Table II. It would be better to verify whether the current density for each sample decays exponentially with T as well or not. If so, as described in the previous reports for some high-T_c superconductors,[15,47] the results indicate the presence of superconducting grains separated by a weak link. A previous study[47] shows that the presence of weak links reduces the J_c value due to the current passing through Josephson junctions.

In Fig. 14, $J_c(H)/J_c(0)$ for $x = 0.05$ behaves differently when compared to the other, as explained in the text. The inset presents J_c (T =5 K, H =0) versus x, the critical current density, J_c increases linearly with T. To give further support to the collective vortices dynamic, the normalized pinning force, $F_p/F_{p,max}$ as a function of the reduced field $h=H/H_{irr}$. Here, we define the irreversibility field H_{irr} at which $J_c(H)$ extrapolates to zero from the field closure of hysteretic magnetization loops (as described below). Figure 15 shows $F_p/F_{p,max}$ versus h ($= H/H_{irr}$) at $T = 5$ K for the sample of $La_{0.95}Ba_{0.05}Pt_{0.1}Fe_{1.9}As_2$.

Here, H_{irr} is estimated from the field closure of hysteretic magnetization loops after subtracting reversible paramagnetic component (see Fig. 13a) to be ~ 12 T. We observe a second magnetization peak (SMP), which is associated with collective vortex behaviors. For example, Krusin-Elbaum et al.[48] described the fishtail effect as a change in magnetization relaxation due to the crossover from single vortex to collective pinning. It is well known that the SMP is closely related to the property of an elementary pinning center. There is a number model suggested for this effect [48, 49, and references therein]. We have used Eq. 4 to fit the data. The fit of $F_p/F_{p,max}$ for the SMP yields the prefactor A_0 = 16.2, $p = 1$, $q = 2$, $\mu CS_0 = -2.75$ with $\mu = 1/7$, $\alpha = 1.95$, and the background $j_0 = -2.7$. As described above, we assume that $S \propto exp\ (-\alpha/h)$ possess a similar reason as mentioned above (since $S \propto (J_c/J_{c0})^{\mu}$ and thermal agitation of the pinning centers at higher fields become dominant) to introduce

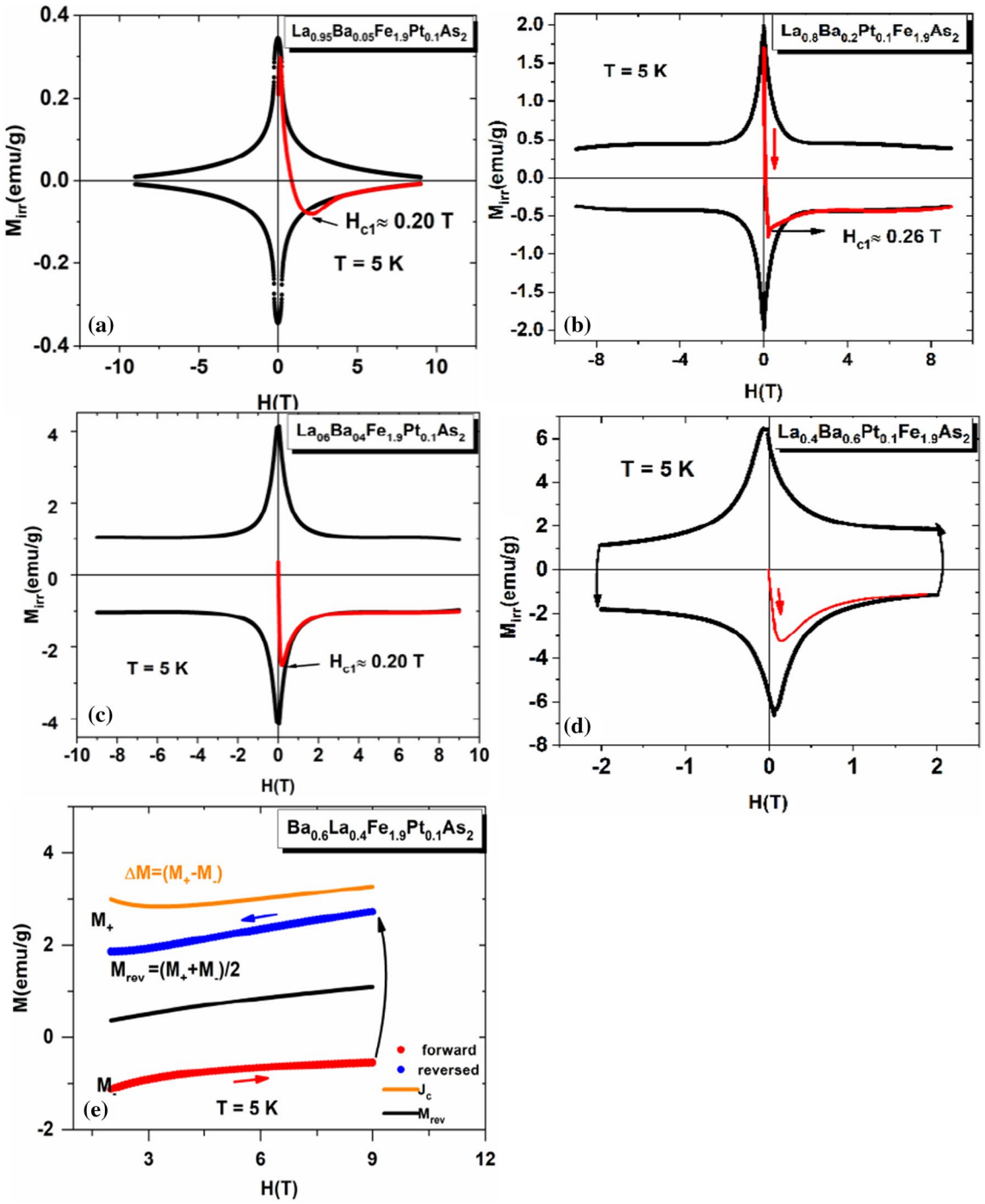

Fig. 13 The M_{irr} versus H at $T = 5$ K in between $H = \pm 9$ T for the $La_{1-x}Ba_xPt_{0.1}Fe_{1.9}As_2$ ($x = 0.05$, 0.2, and 0.4) compounds after subtracting the paramagnetic contribution from M measured as described in the text, presented as Fig. 13a, b, c, and Fig. 12d for $x = 0.05$, 0.2, 0.4, 0.6, respectively.

this term. This can improve the quality of fitting, as seen in Fig. 15.

Note that a change from single vortex creep to collective vortex creep with increasing field sets on $h_{on} \approx 0.05$ T is indicated in the figure. The relaxation rate, *S,* passes through a maximum at $h_{e\text{-}p} \approx 0.5$ T, where the transition from elastic to plastic state may take place. Indeed, instead of using one unique function, including two peaks in the fitting, each peak fitting was performed separately. To reduce the number of fitting parameters, we could use the results obtained from the separate fitting. Instead, the fitting parameters of S are plotted in the same figure, and then we combine them to get

Table I Fitting of the M_{rev} versus H at $T = 5$ K using the Langevin equation for the samples of $La_{(1-x)}$ $Ba_xPt_{0.1}Fe_{1.9}As_2$ ($x = 0.05$, 0.20, 0.40, and 0.60). The fitting parameters M_s, M_0, μ_s, and μ_{eff} are listed

Sample	M_s (emu/g)	μ_s (μ_B/f.u)	μ_{eff} (μ_B/ion)	M_0 (emu/g)
$La_{0.95}Ba_{0.05}Pt_{0.1}Fe_{1.9}As_2$	8.67	0.64	1.80	0.46
$La_{0.8}Ba_{0.2}Pt_{0.1}Fe_{1.9}As_2$	5.77	0.43	2.23	0.40
$La_{0.6}Ba_{0.4}Pt_{0.1}Fe_{1.9}As_2$	3.69	0.27	2.22	0.36
$La_{0.4}Ba_{0.6}Pt_{0.1}Fe_{1.9}As_2$	1.5	0.12	2.22	0.16

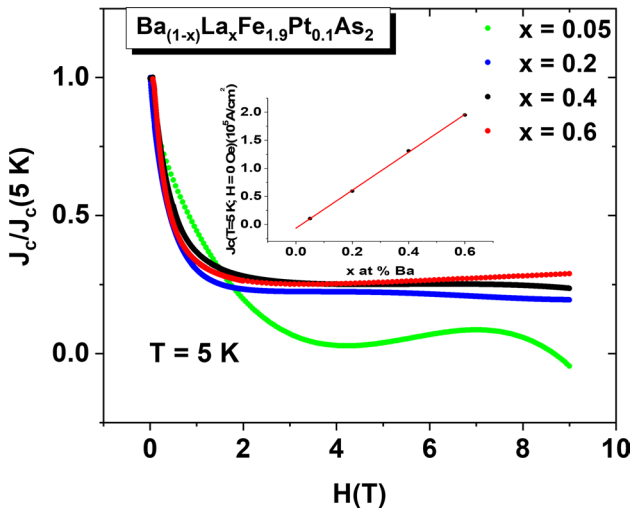

Fig. 14 The critical current density, J_c (H, T= 5 K) normalized to its value at $H = 0$, $J_c(0, T = 5$ K), $J_c(H)/J_c(0)$ versus H at $T = 5$ K for the $La_{1-x}Ba_xPt_{0.1}Fe_{1.9}As_2$ (x =0.05, 0.2, 0.4, and 0.6) compounds.

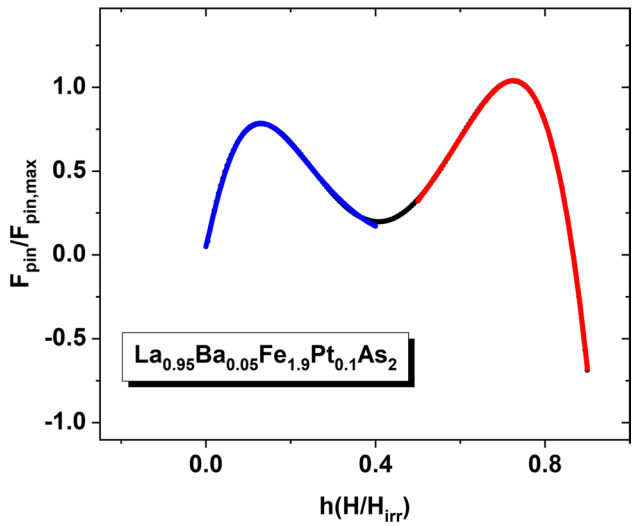

Fig. 15 The normalized pinning force density, $F_p/F_{p,max}$, curves versus $h=H/H_{irr}$ (H_{irr} is the irreversibility field) at $T = 5$ K is plotted sample of $La_{0.95}Ba_{0.05}Pt_{0.1}Fe_{1.9}As_2$. Note that $F_p/F_{p,max}$ exhibits two separate magnetization (SM) peaks. Data were scaled using the Dew-Hughes model. The continuous line indicates the fits with different colors with SM peaks.

Table II The critical current density normalized to its value at $T = 5$ K, $J_c(H)/J_{c0}$ is fitted to the empirical expression, $J_c(H)/J_{c0} = j_0 + a.exp(-H/H_0)$ for the samples of $La_{1-x}Ba_xPt_{0.1}Fe_{1.9}As_2$ (x =0.05,0.20,0,40, and 0.60). The fitting parameters, j_0, a, and H_0 are listed

Sample	A_0	k_1	k_2(T)	α
$La_{0.95}Ba_{0.05}Pt_{0.1}Fe_{1.9}As_2$	0.43	$1.7x10^{-6}$	0.0082	2.57
$La_{0.80}Ba_{0.20}Pt_{0.1}Fe_{1.9}As_2$	3.38	3.32	0.020	0.009
$La_{0.60}Ba_{0.40}Pt_{0.1}Fe_{1.9}As_2$	7.78	3.03	0.625	0.0123
$La_{0.40}Ba_{0.60}Pt_{0.1}Fe_{1.9}As_2$	11.15	2.03	0.35	0.29

a common curve in the entire range of $h(=H/H_{irr})$. Thus, using such a simple way, we could get the field dependence of the logarithmic relaxation rates $S=-(1/M)$ $(dM/dlnt)$ determined at 5 K. As shown in Fig. 16, S passes a through a minimum at h_{on} =0.05 where a collective creep mechanism starts (note that the pinning energy U does not depend on field below h_{on}) and then increases with the field, reaches a maximum at a field $h_{e\text{-}p}$ =0.5 and then slows down where it takes a phase transition from an elastic vortex state to a plastic vortex.[45,50,51] As a result, we conclude that more than

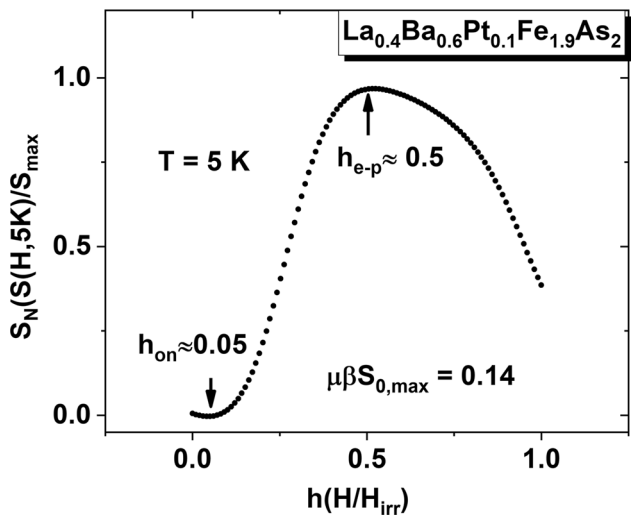

Fig. 16 The field dependence of relaxation rate, S (H, T) normalized to its maximum value, S_{max} in the range of $0<h<1$ at $T = 5$ for $La_{0.4}Ba_{0.6}Pt_{0.1}Fe_{1.9}As_2$.

one pinning mechanism may be operating in this material. Their effects will add and produce a new pinning function; thereby, different mechanisms govern the shape of $F_p/F_{p,\,max}$ curve. $J_c(H)$ at $T = 5$ K was analyzed within the collective pinning model at low fields for $La_{0.8}Ba_{0.2}Pt_{0.1}Fe_{1.9}As_2$, $La_{0.6}Ba_{0.4}Pt_{0.1}Fe_{1.9}As_2$, and $La_{0.4}Ba_{0.6}Pt_{0.1}Fe_{1.9}As_2$. Under the collective pinning model,[15] $J_c(T)/J_{c0}$ $(5K)$ versus H curves were evaluated, and the related fitting parameters were obtained by using Eq. 3 and listed in Table III.

It must be borne in mind that careful measurement of J_c versus H over as wide a temperature range as possible is required to compare the predicted pinning functions with experimental findings. We assume that $H_{c2} \approx H_{irr}$, an accurate determination of H_{c2} is usually estimated by extrapolation of J_c versus H to $J_c = 0$. It is common to make a linear extrapolation, or it is more appropriate to extrapolate $J_c^{1/2}$ versus H. It is also worth noting that there is a remarkable difference in the field dependence behavior of J_c/J_{c0} between the sample for x =0.05 Ba content and those for the others x= 0.2, 0.4, and 0.6, as shown in Fig. 14. $J_c(H)$ behavior closer to exponential decay $A\ exp(-H/H_0)$ rather than a power-law decay $H^{-\alpha}$ (which is consistent with strong pinning theory predictions) is observed in x =0.2, 0.4, and 0.6 samples covered the measurement field range 0-9 T. While we observe an exponential decay for $x = 0.05$, in J_c at H< 30 T, but, at higher fields, it exhibits a rounded maximum located at $H \sim 7$ T (h =0.7, $H_{irr} \sim 10$ T) to the second magnetization peak (SMP) as described above, which allows us to determine an accurate determination of H_{irr} for this composition at $T = 5$ K. However, we fail to reveal the pinning mechanism at higher fields for the other compounds at this temperature because the accurate interpretations in this respect are only possible by knowing the exact determination of the irreversibility field H_{irr}. To demonstrate the difficulty, we also present $M(H)$ curve separately at 5 K in higher field sides, as seen in Fig. 10e. As shown in the figure, it appears that the irreversibility will take place at much higher fields than our highest measurement field 9 T.

The only way to determine the H_{irr} is to perform the magnetization measurements at higher temperatures below T_{sc}. The M vs. H measurement at T_{sc} =24 K in between H =±9 T for $La_{0.4}Ba_{0.6}Pt_{0.1}Fe_{1.9}As_2$ is performed. Its irreversible component, M_{irr} vs. H, obtained from the M vs. H curve after subtracting the reversible component, M_{rev} is plotted in Fig. 17. Please see also M-H, M_{rev} vs. H, and J_c/J_{c0} vs. H presented in the insets of Fig. 17. The fit to Eq. 4 yields the best-fitting parameter values. These are k_1 =0.66, k_2 =0.9 T, $\alpha = 0.23$, and $J_c(0) = 22.5$ A/cm^2.

Note that $F_p/F_{p,max}$ exhibits two separate second magnetization (SM) peaks. The continuous red line presents the fit to the Eq. 4 is described in the text. Note that the second magnetization peak is relatively weak. The accurate determination of the irreversibility field will enable us to provide the field dependence of the pinning force normalized to its maximum value, $F_p/F_{p,max}$ at this temperature (see Fig. 18). It should be noted that two peaks are superimposed, but both are evident in Fig. 18. The peak on the high field side gives the second magnetization peak, which is relatively too weak, inappropriate for fitting. We only evaluate the peak located at the lower field side. The fitting parameters (extracted after fitting the low-field side data to Eq. 4 used) are $A_0 = 14.1$, $p = 1$, q =2, $\mu CS_0 = 0.13$ with $\mu = 1/7$, α=0.86, $n = -2.16$ and the background j_0 = -0.025. As described above, we assume that $S \propto h^n exp(-\alpha/h)$ possesses a similar reason as mentioned above. This pinning corresponds to normal point pins. In fact, there are usually two types of pinning centers to be referred to as '$\Delta\kappa$ pinning' and 'normal pinning'. The values of these parameters suggest point pins whose dimensions in all directions are less than the inter-flux line spacing $\left(d^2/\sqrt{3}(\varphi_0/B^{1/2})\right)$ where φ_0 denotes the flux

Table III Normalized current density to its value at T = 5 K to the empirical equation $J_c(H)/J_{c0} = 1/\,[1 + k_1 exp(-k_2/H)\,(H/k_2)^{\alpha}]$. The fitting parameters, J_{0c}, k_1, k_2, and α are listed for the samples of $La_{(1-x)}Ba_xPt_{0.1}Fe_{1.9}As_2$. (x =0.05, 0.20, 0.40, and 0.60)

Sample	J_0	a	H_0 (T)
$La_{0.95}Ba_{0.05}Pt_{0.1}Fe_{1.9}As_2$	-0.001	0.022	1.54
$La_{0.80}Ba_{0.20}Pt_{0.1}Fe_{1.9}As_2$	2.11	6.46	2.67
$La_{0.60}Ba_{0.40}Pt_{0.1}Fe_{1.9}As_2$	2.16	6.56	0.48
$La_{0.40}Ba_{0.60}Pt_{0.1}Fe_{1.9}As_2$	3.12	9.87	0.34

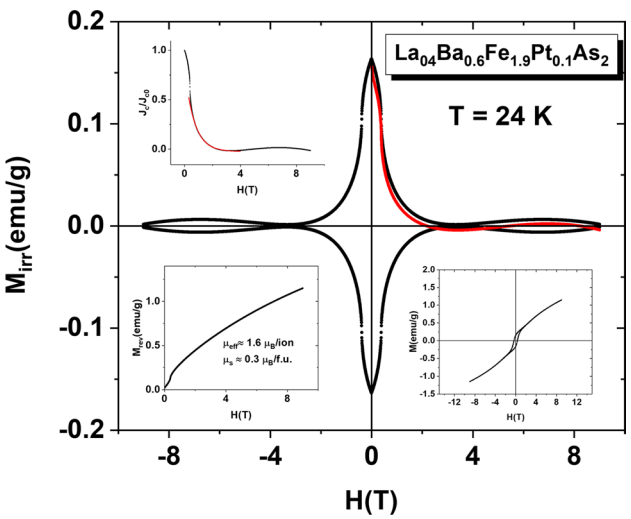

Fig. 17 M_{irr} versus H at $T = 24$ K in between $H = \pm 9$ T for the $La_{0.4}Ba_{0.6}Pt_{0.1}Fe_{1.9}As_2$. Note that the initial magnetization curve was given by the continuous red line. The lower inset on the right presents M versus H at $T = 24$ K between $H = \pm 9$ T. The upper inset on the left displays J_c/J_{c0} versus H. The red line is the best fitting curve to Eq. 4 in the text.

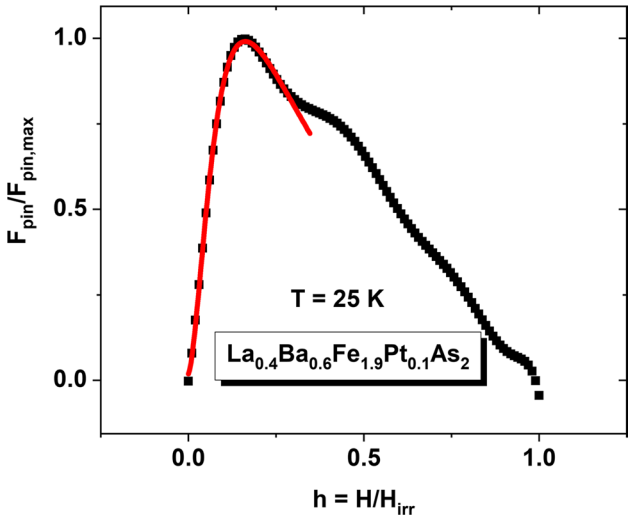

Fig. 18 The normalized pinning force density, $F_p/F_{p,max}$, curves versus $h=H/H_{irr}$ (H_{irr} is the irreversibility field) at $T = 24$ K is plotted for the sample of $La_{0.4}Ba_{0.6}Pt_{0.1}Fe_{1.9}As_2$.

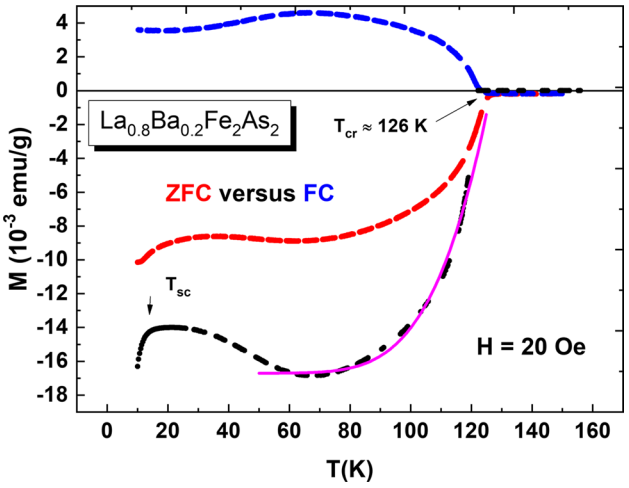

Fig. 19 M_{ZFC} versus M_{FC} at $H = 20$ Oe in the temperature range, 5 K<T<300 K. The lower curve is the initial magnetization data recorded during cooling the sample to 5 K, in the very small field estimated to be ~ 1 Oe (remnant field of the magnet).

quantum, B is the magnetic induction field in the sample. Since small and point-sized defects limit the mean free path, l, of the conduction electrons, the vortex pinning in this sample can be attributed to δl-type pinning.

The magnetic and electric properties of $La_{0.8}Ba_{0.2}Fe_2AS_2$ compound have been investigated exclusively to explore the role of Ba (hole-doped in an indirect way) in the superconducting properties. Temperature-dependent magnetization curves measured in the ZFC, FC conditions in the presence of $H = 20$ Oe are shown in Fig. 19. The initial magnetization data are also recorded during cooling the sample from the room temperature to 5 K in the remnant field of the magnet (the residual magnetic field is the field that remains in the magnet after the current is turned off, which is estimated to be ~ 1 Oe) (indicated by black symbols in Fig. 19).

It should be noted that MZFC drops sharply at around 126 K and exhibits a giant diamagnetic magnetization. The continuous line is the fitting curve using the empirical equation $M = M_{dia}+M_1 exp(-\Delta/T)$ as described in the text.

The kink observed in this curve can be associated with the onset (indicated by arrow) of the bulk superconducting transition at T_c ~ 14 K, at which the resistivity shows a sharp drop (see Fig. 26). The volume fraction of superconductivity at T=5 K is estimated to be approximately 27 %. The other phase transition occurs at around $T = 126$ K (indicated by another arrow in the figure), which seems to be associated with the cluster frozen processes.[32] It should be noted that a giant diamagnetism is observed in the ZFC condition and FC unless the cooling field, H_c is much greater than the coercive field, H_{coer} of the sample, implying that the sample is cooling in its internal field or other words the effective magnetic field, H_{eff} seen by clusters is almost zero. Indeed, we use $M = M_{dia} + M_1 exp(-\Delta/T)$ to fit the M data, yielding $M_{dia} = -0.0167$ emu/g , $M_1 = 13$ emu/g, and $\Delta = 860$ K. The fitting quality is quite satisfactory. In fact, the freezing transition is a quite general phenomenon and thus applicable to a diverse range of systems, such as spin glasses via (say) the random energy model. The theory of thermal activation plays a central role, in which the rate at which a particular $<M_{eq}>$ occurs is given by the product of an attempt rate ν_i, and the probability that such an attempt is successful, $exp(-\beta\Delta E_i)$, which is characterized by an energy barrier $\Delta E_i = k_B \Delta$ and temperature $\beta = 1/k_B T$. As for M_{dia} used in magnetization can be attributed to the frozen domain pairs. As pointed out by the Buzdin group,[52] perhaps the domain walls may generate superconducting vortices in the domains.

We have also demonstrated the Meissner state of this compound at T =5 K. Figure 20 shows M_{irr} versus H curve between in $H = \mp 0.05$ T. From the same M data, as described above, The normalized pinning force to its maximum value as a function applied magnetic field, $F_{pin}/F_{pin,max}$ versus h (H/H_{irr}), has been plotted in Fig. 21. Using Eq. 4, the best values of the fitting parameters are obtained as follows $A_0 = 3.27$, $p = 0.5$, q =2, $\mu CS_0 = 0.333$ with $\mu = 1/7$, h_0=0.017 T [here, we used $exp(-h_0/h)$ term instead of $exp(-\alpha h)$], n = -0.216 and the background $j_0 = 0.36$. The fitting parameters obtained from the fitting lead us to suggest that normal surface flux pinnings occur on the interfaces of grain boundaries (or on the domain wall surfaces).

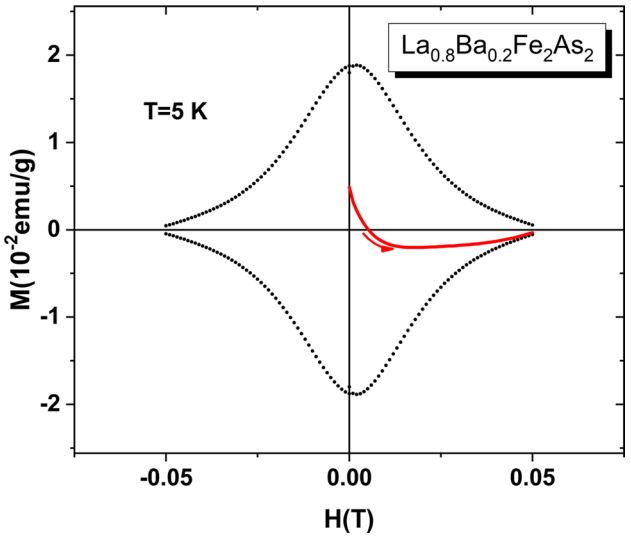

Fig. 20 M_{irr} versus H at T = 5 K between $H = \mp 0.05$ T for the $La_{0.80}Ba_{0.20}Fe_2As_2$. Note that the continuous red line gives the initial magnetization curve.

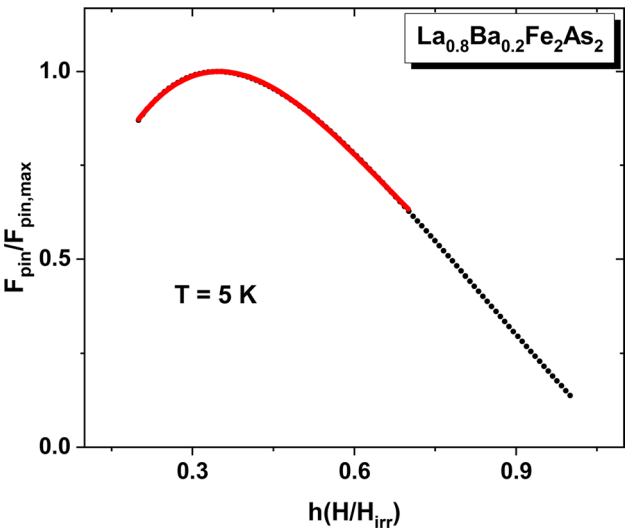

Fig. 21 The normalized pinning force density, $F_p/F_{p,max}$, curves versus $h=H/H_{irr}$ at T = 5 K is plotted for the sample of $La_{0.80}Ba_{0.20}Fe_2As_2$. The continuous line indicates the fitting data.

Resistivity Analysis

The resistivity measurements have been carried out on the samples of $LaFe_2As_2$, $La_{1-x}Ba_xPt_{0.1}Fe_{1.9}As_2$ (x = 0, 0.05, 0.2, 0.4, and 0.6) in the temperature range of 5 – 300 K. Figure 22 shows the temperature dependence of resistivity for the samples with different x values. In the nanoscale range, all of the samples transition from a high-temperature spin disordering (or partly ordering) state to a low-temperature spin ordering (ferromagnetic-like) state. However, in a larger scale range, we observe superparamagnetic-like behavior as described above. In the normal state, the resistivity data is divided into two regions: the lower temperature range takes place between T_c and T_m where the resistivity change the slope (note that the mean free path of the conduction electrons is about a few angstroms in over the entire temperature range), the other is considered to cover the range of temperatures, $T_m \leq T < 300$ K.

Figure 22a shows the resistivity, ρ(T) for the collapsed tetragonal phase of $LaFe_2As_2$ (CT-La122) taken from the paper published by Iyo et al. (see Ref 18). The superconducting phase transition, T_{sc} is estimated to be as 14 K indicated in the figure. T_{sc} for each sample is also estimated in a similar way and indicated in the figure. The continuous blue lines are the fitting curves using $\rho = \rho_0 + AT^n$ (T-power law) in low-temperature range; the continuous red lines are the fitting curves using $\rho = \rho_0 + \rho_1 T + \rho_2(1/T)\, exp(-\Delta/T)$ expression in the high-temperature range for all samples. Insets present the temperature derivative of the resistivity, $d\rho/dT$ *vs.* T. It passes through a maximum at T_m where a magnetic transition from paramagnetic phase to magnetic ordering phase is observed.

We find that the resistivity of all the samples except $La_{0.4}Ba_{0.6}Pt_{0.1}Fe_{1.9}As_2$ is well described by the temperature dependence of the form $\rho(T) = \rho_0 + AT^n$. The best values of the fitting parameters are listed in Table IV.

The resistivity of the $LaFe_2As_2$ sample just above the superconducting transition follows almost perfectly a linear temperature dependence. The other doped sample displays a T^2 dependence or close to the quadratic behavior as expected for a Fermi liquid at low T in terms of a single band picture, despite the multiband nature of the electronic structure predicted for the Fe based superconductors. The observation of T^2 behavior at such elevated temperatures indicates the presence of strong electronic correlations. The linear temperature behavior of the resistivity in $LaFe_2As_2$ may be associated with their two-dimensional character for electron transport as commonly observed in high-T_c cuprate[53] and previously reported in some Fe-based superconductors [54, and references therein] as well. It is also noticed that with the increasing Ba content, the resistivity deviates slightly from the T^2-dependence. These findings impose new constraints on the mechanisms responsible for inelastic scattering of the conduction electrons and Fermi-surface transformation in the Ba-doped $LaFe_2As_2$ system. Note also that the residual resistivity, ρ_0 increases linearly with the increasing Ba content, x from 37 μΩ cm for x =0.05 to 117 μΩ cm for $x = 0.40$. It may be attributed to the atomic disordering induced by Ba content, apart from also lowering the electron charge carrier density.

At higher temperatures, we adapted the following empirical expression to describe the resistivity data, as suggested

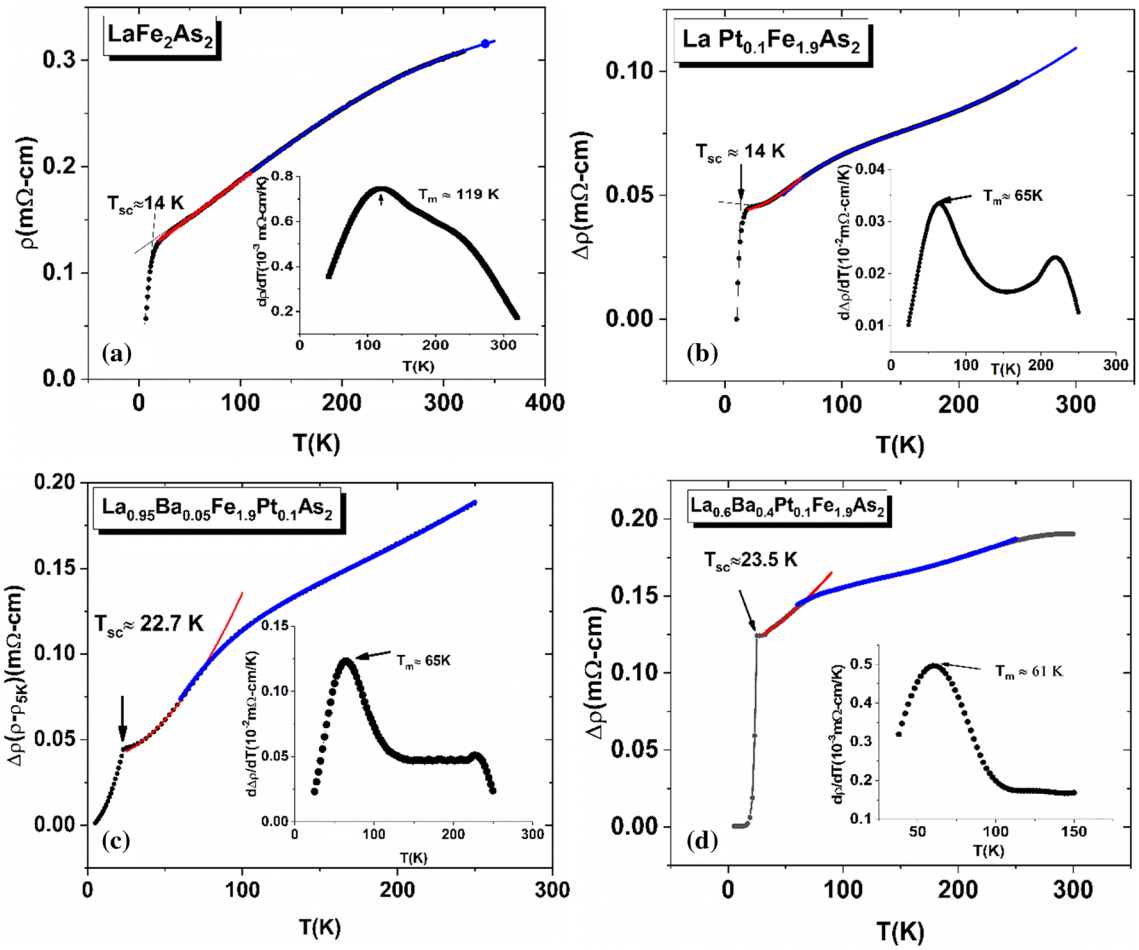

Fig. 22 Resistivity as a function of the temperature for the $LaFe_2As_2$ and $La_{1-x}Ba_xPt_{0.1}Fe_{1.9}As_2$ ($x = 0$, 0.05, 0.2, and 0.4) compounds introduced by (a), (b), (c), and (d), respectively.

Table IV The resistivity $\rho(T)$ is fitted to the empirical expression for the sample of $LaFe_2As_2$ and $La_{1-x}Ba_xPt_{0.1}Fe_{1.9}As_2$(x =0, 0.05, 0.20, 0.40, and 0.60), $\rho = \rho_0 + AT^n$. The fitting parameters ρ_0, A, and n are listed

Sample	ρ_0 (x10^{-2}mΩ cm)	A (x10^{-6}mΩ cm $K^{-\alpha}$)	n
$LaFe_2As_2$*	11.6	71	1.0
$LaPt_{0.1}Fe_{1.9}As_2$	4.3	0.34	2.0
$La_{0.95}Ba_{0.05}Pt_{0.1}Fe_{1.9}As_2$	3.7	0.98	2.0
$La_{0.80}Ba_{0.20}Pt_{0.1}Fe_{1.9}As_2$	7.6	0.72	1.8[5]
$La_{0.60}Ba_{0.40}Pt_{0.1}Fe_{1.9}As$	11.7	1.91	1.7[5]

by Gasparov et al.[55] for the system of K-doped $BaFe_2As_2$ compounds.

$$\rho(T) = \rho_0 + \rho_1 T^{\alpha} + \rho_2 (1/T)\, exp\,(-/T) \tag{6}$$

It is noted that α varies within the range $1 \leq \alpha \leq 2$. The first two terms are closely related to those obtained for the low temperature-side region. It is found that the adding of the second exponential term together with $(1/T)$ prefactor well describes the resistivity above T_m. The fitting temperature ranges are indicated in the figure for each sample. The best-fitting value for the fitting parameters, ρ_0, ρ_1, ρ_2, α, and Δ are given for each sample in Table V.

In fact, Wilson[56] first suggested the exponential term in the above equation arising from interband electron-phonon umklapp scattering from a low-mass s-band sheet to a heavy-mass d-band sheet for Nb_3Sn. The freezing out of these processes at low temperatures is responsible for the exponential dependence of $\rho(T)$. Then, such a scenario for electron-phonon umklapp scattering between a small and large Fermi-surface sheet was considered by some low-temperature superconductors such as Nb_3Sn. In this model, $\Delta = \hbar\, \Delta\, ks/k_B$ is the temperature at which the averaged phonon wave vector q is equal to the inter-sheet distance Δk, s is the sound velocity, and k_B the Boltzmann constant. For our

Table V The resistivity $\rho(T)$ is fitted to the emprical expression for the sample of $LaFe_2As_2$ and $La_{1-x}Ba_xPt_{0.1}Fe_{1.9}As_2$ (x =0, 0.05,0.20, 0.40, and 0.60), $\rho = \rho_{0+}\rho_1 T^{\alpha} + \rho_2 exp(-\Delta/T)$. The fitting parameters, ρ_0, ρ_1, Δ, and α are listed

Sample	ρ_0 (x10^{-2}mΩ cm)	ρ_1 (x10^{-6}mΩ cm $K^{-\alpha}$)	ρ_2 (mΩ cm K)	Δ(K)	α
$LaFe_2As_2$*	17	115	166	525	2.1
$LaPt_{0.1}Fe_{1.9}As_2$	3.8	0.6	10	150	1.6
$La_{0.95}Ba_{0.05}Pt_{0.1}Fe_{1.9}As_2$	3.8	1.27	36	174	1.93
$La_{0.80}Ba_{0.20}Pt_{0.1}Fe_{1.9}As_2$	7.1	1.26	12	143	1.82
$La_{0.60}Ba_{0.40}Pt_{0.1}Fe_{1.9}As$	12	1.87	8.2	118	1.82
$La_{0.40}Ba_{0.60}Pt_{0.1}Fe_{1.9}As$	63.7	2.43	255	70	1.82

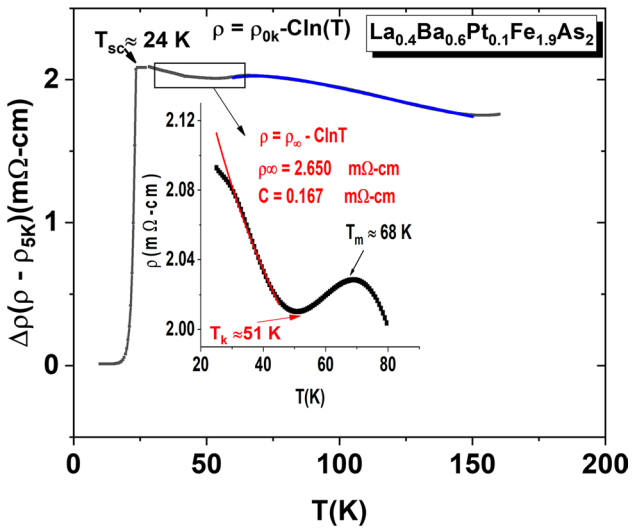

Fig. 23 Resistivity as a function of the temperature for the sample of $La_{0.4}Ba_{0.6}Pt_{0.1}Fe_{1.9}As_2$. Two temperature regions above T_{sc} are evident: one ranges between $T_{sc} \approx 24$ K and $T_m \approx 68$ K, the other above T_m. The continuous blue line is the fitting curve using $\rho = \rho_0 + \rho_1 T + \rho_2(1/T)\ exp(-\Delta/T)$ expression in the high-temperature range as described in the text. Below T_m, a resistivity minimum is observed at $T_k \approx 51$ K, referred to as the Kondo minimum. $\rho = \rho_\infty - Cln(T)$ expression is used for the fitting above T_k (the continuous red line presented in the figure of the inset). Inset shows the resistivity data in the range $T_{sc}<T<T_m$ on an expanded scale.

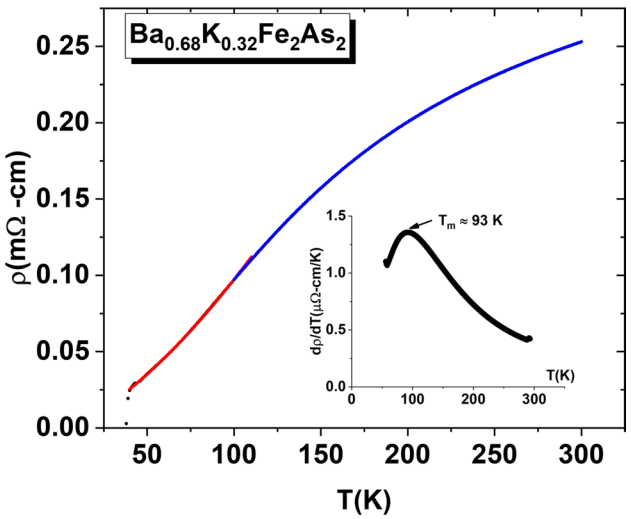

Fig. 24 The temperature dependence of the resistivity, $\rho(T)$ for $Ba_{0.68}K_{0.32}Fe_2As_2$ introduced from Ref. 55 (see Fig. 1 in this reference). The inset shows the temperature derivative of ρ, $d\rho/dT$ versus T. It passes through a maximum at T_m, the Neel temperature, T_N of $Ba_{0.62}K_{0.38}Fe_2As_2$.

system, Δk may correspond to the nesting vector between d-holes and electron pockets. It is widely believed that spin fluctuations due to interband electron-hole scattering play a crucial role not only in the superconducting pairing but also in normal transport.[57] However, rigorous theoretical approaches are required to clarify these assertions. It should be noted that the parameter Δ decreases with x by the relation $\Delta = \Delta_0(1-x)$ where Δ_0=183 K. It is interesting to note that the linear increase of T_c with x seems to be highly correlated with the linear decrease in the energy gap Δ.

It is also noted that $La_{0.4}Ba_{0.6}Pt_{0.1}Fe_{1.9}As_2$ exhibits a Kondo effect, as seen in Fig. 23. The resistivity data below T_k=51 K is well described by the $\rho = \rho_\infty - ClnT$. The fitting parameters are indicated inn the inset in Fig. 22d. Similar behavior has already been observed in the epitaxial thin films of $Ba_{1-x}La_xFe_2As_2$ (x = 0.13 and 0.18) and reported previously [for further detail see Ref. 58]. Finally, we would like to point to a certain similarity in the temperature behavior of the resistivity in $Ba_{1-x}K_x122$ and $La_{1-x}Ba_x122$ superconductors. By substituting Ba^{2+} for La^{3+} ions, we have introduced holes in $LaFe_2As_2$, while by substituting Ba^{2+} for K^+ ions, one can introduce holes in the $BaFe_2As_2$ system. Both parent components have the same crystal structure. So, it is expected to find similarities in the temperature behavior of their resistivity between these systems.

The resistivity data in Fig. 24 were fit to different empirical expressions [$\rho = \rho_0 + aT^n$ and $\rho = \rho_0 + \rho_1 T^2 + \rho_2(1/T)\ exp(-\Delta/T)$] below, and above T_m, the fitting curves are indicated by continuous blue and red lines, respectively. Indeed, when we introduced the resistivity curve of $Ba_{0.62}K_{0.38}Fe_2As_2$ from Gasparov's paper[55] (see Fig. 24), we find that this compound behaves in the same way as far as the temperature dependence of their resistivity is concerned. It should be noted that $T_m \approx 93$ K indicated in the inset of Fig. 24, where the $d\rho/dT$ passes through a maximum, which has taken as the Néel

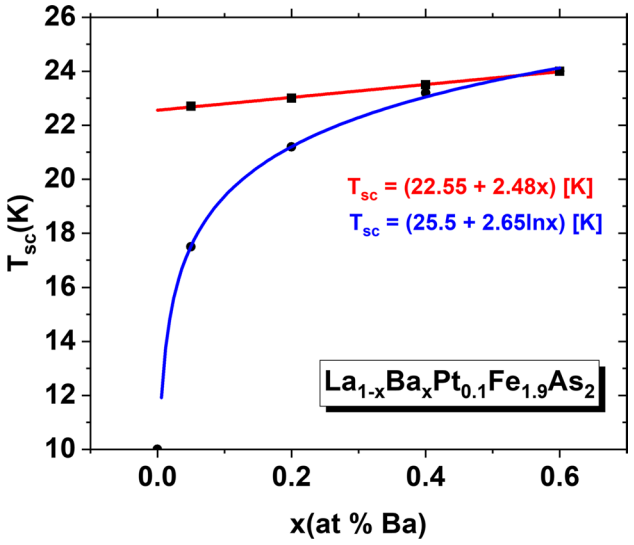

Fig. 25 The superconducting transition temperature, T_{sc} as a function of doping concentration, x. Note that T_{sc} determined from resistivity increases linearly with x, well described by T_{sc} = *22.55+2.48x* [K], but logarithmically with x, T_{sc} =*25.5 + 2.65lnx* [K] when it was determined from magnetization measurements

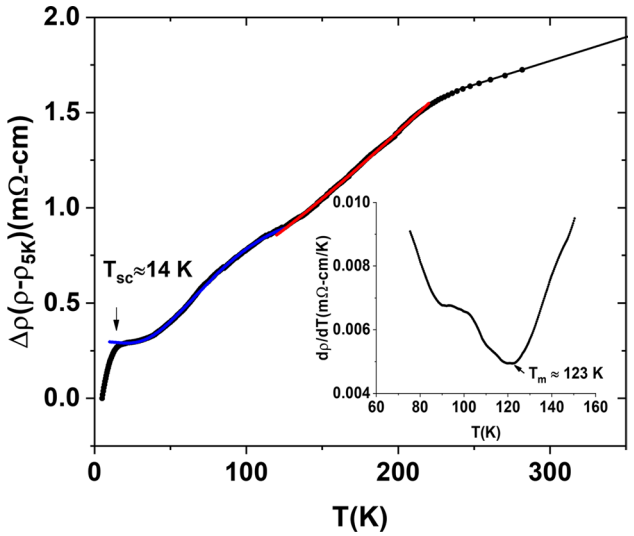

Fig. 26 Resistivity as a function of the temperature for the samples of $La_{0.80}Ba_{0.20}Fe_2As_2$). The superconducting phase transition, T_{sc} is estimated to be 14 K as indicated by an arrow in the figure.

temperature, T_N for this compound. However, Avci et al. for x >0.2 reported[59] that the magnetization anomaly at T_N is too weak to be detected in their magnetization study using SQUID. We believe that the cluster (or domain) frozen effects at higher K doping result in such peculiar behavior. We believe that the resistivity measurement technique presumably would be better as a microscopic probe to reveal the antiferromagnetic phase transition, owing to detect the spin ordering in the microscopic scale since the mean free path of the conduction electrons is about 10-50 Å ($\rho \approx a$ few mΩ cm in normal state).

It is also interesting to note that the superconducting transition temperature, T_{sc} determined from the magnetization measurements, which does not coincide precisely with that of obtained values from the resistivity measurements. From the electrical resistivity measurements, it is found that T_{sc} increases linearly with increasing Ba doping concentration x; namely, it is well described by T_{sc} =*22.55 + 2.48x* [K], whereas, from the magnetization study, it is seen that T_{sc} increases logarithmically with x given by the relation of T_{sc} =*25.5 + 2.65lnx* [K], as shown in Fig. 25. This difference can be explained by the fact that the resistivity measurement is microscopic; that is, it is very sensitive to the change in the magnetic state within the microscopic scale.

We also introduce the resistivity data of the compound $La_{0.8}Ba_{0.2}Fe_2As_2$ in the temperature range of 5–300 K. As shown in Fig. 26, there are many aspects of the data that require detailed temperature analysis.

In Fig. 26, the continuous blue lines are the fitting curves using $\rho = \rho_0 + \rho_1 T^2 + \rho_2 \, exp\,(-\Delta/T)$ in the low-temperature range (20 K<T<126 K), the continuous red lines are the fitting curves using $\rho = \rho_0 + ATexp(-\Delta/T)$ expression in the high-temperature range (126 K<T<220 K). Insets present the temperature derivative of the resistivity, $d\rho/dT$ vs. T. It passes through a maximum at T_m where a magnetic transition from the paramagnetic phase to magnetic ordering phase is observed.

It seems to us likely that the same empirical expression used in similar compounds with thin films[56] can account for the resistivity data in this compound. According to this study, in the temperature range in $T_{sc}<T<T_m$ the resistivity changes its slope at T_m, shown in the inset of Fig. 26. The resistivity, ρ can be written as a sum of two competitive terms: $\rho = \rho_0 + \rho_1 T^2 + \rho_2 exp(-\Delta/T)$, the first term acts as $\rho_c(1-\alpha T^2)$, implying that the resistivity increases with decreasing temperature due to the spin fluctuations (or Kondo effect); [60,61] the second term is associated with interband scattering. The exponential term was first suggested by Wilson[56] since there are two pockets to this Fermi surface for our system [one pocket near k=0 (the Γ point) and one pocket near k= (π, 0) (the M point); tThese two pockets are said to be nested], we have very recently suggested that this exponential term is closely related to the nesting vector between d-holes and electron pockets.[58] The fitting parameters are $\rho_0 = 0.3$ mΩ cm, $\rho_1 = -2.6 \times 10^{-5}$ mΩ cm/K^2, ρ_2 =3.27 mΩ cm, and Δ =148 K. It is noticed that the second term becomes dominant over the first term. Otherwise, it would exhibit a resistivity minimum at this compound, as observed in thin films of similar compounds.[58] As for the resistivity at temperatures above T_m, the following empirical expression gives a perfect fit: $\rho = \rho_0 + ATexp\,(-\Delta/T)$. This expression has already been used

by many authors[62] in 122 Fe pnictide superconductors. It is generally introduced in order to describe the universal superlinear resistivity $\rho(T)$. The above empirical formula yields the best fitting parameters values in the temperature range, $T_m<T<220$ K was obtained as $\rho_0 = 0.5$ mΩ cm, $A = 8.5x10^{-3}$ mΩ cm/K, and $\Delta = 128$ K. Above 220 K, the fitting deviates more and more from the superlinear temperature behavior to the normal linear T behavior. As a result, we can conclude that only hole-doped $LaFe_2As_2$ provides significantly different temperature behavior of resistivity compared to electron-doped samples. This is due to electron and hole doping to $LaFe_2As_2$ resulting in different electron and hole pockets Fermi surface topologies as expected.

Conclusion

Novel superconductors $La_{1-x}Ba_xPt_{0.1}Fe_{1.9}As_2$ (x =0, 0.05, 0.2, 0.4, and 0.6) were synthesized for the first time by using a conventional solid-state reaction method with substitution of a small amount of Pt (nominal ~1 at %) at Fe sites and divalent Ba for trivalent La in $LaFe_2As_2$. All the samples are well crystallized under the same conditions in the $ThCr_2Si_2$-type structure with a space group of *I4/mmm*.

1. As prepared, the $LaFe_2As_2$ sample in the normal state consists of a large number of smaller and similar magnetic domains developed by the thermal agitation under the internal magnetic field during the cooling process. It becomes a superconductor with $T_{sc} \approx 14$ K (measured from the resistivity measurements). Based on the implication of the pinning force F_p analyses, we conclude that the superconductivity has a predominantly percolated filamentary character occurring on the domain surfaces.

2. Ba^{2+}substitution for La^{3+} produces a bulk superconductivity in $La_{1-x}Ba_xPt_{0.1}Fe_{1.9}As_2$ (x =0, 0.05, 0.2, 0.4, and 0.6) with a maximum T_c of ~24 K at $x \approx 0.6$. Superconducting volume fraction increases gradually with x. Its maximum value obtained by magnetic susceptibility measurement is 100 % for x =0.6.

3. We observe a giant negative diamagnetic susceptibility at about 115 K for all Ba-doped samples, but its origin remains unknown.

4. After subtracting the paramagnetism from the measured M-H curves, the critical current density, J_c, and normalized pinning force $F_p/F_{p,max}$ as a function of the applied field are obtained. Based on the results obtained from these analyses, we claim that the superconductivity in as prepared all the samples occurs on the domain boundary with the filamentary character and bulk superconductivity inside the domains.

5. We revealed that $La_{0.4}Ba_{0.6}Pt_{0.1}Fe_{1.9}As_2$ has a very high $H_{c2,}$ and its critical current density J_c at 4.2 K and 9 T achieves an order of 10^5 A/cm^2, which is suggested for high-field magnet applications.

6. It is likely that the diamagnetism observed in this system is due to the induced ring currents which are localized on the small clusters.[32,63] The strongly enhanced diamagnetism is scaled with the size of the cluster and the large number of electrons involved.

Acknowledgments We convey our thanks to Prof. Dr. Sevda Avci for her useful discussions and Dr. Adil Guler for sample preparation. This research did not receive any financial support.

Conflict of interest The authors declare that they have no conflict of interest.

References

1. Y. Kamihara, T. Watanabe, M. Hirano, and H. Hosono, *J. Am. Chem. Soc.* 130, 3296 (2008).
2. J. Paglione, and R.L. Greene, *Nat. Phys.* 6, 645 (2010).
3. G.R. Stewart, *Rev. Mod. Phys.* 83, 1589 (2011).
4. M. Rotter, M. Tegel, and D. Jorendt, *Phys. Rev. Lett.* 101, 107006 (2008).
5. K. Sasmal, B. Lv, B. Lorenz, A.M. Guloy, F. Chen, Y.Y. Xue, and C.W. Chu, *Phys. Rev. Lett.* 101, 107007 (2008).
6. G. Wu, H. Chen, T. Wu, Y.L. Xie, Y.J. Yan, R.H. Liu, X.F. Wang, J.J. Ying, and X.H. Chen, *J. Phys.: Condensed Matter.* 20, 422201 (2008).
7. X.C. Wang, Q.Q. Liu, Y.X. Lv, W.B. Gao, L.X. Yang, R.C. Yu, F.Y. Li, and C.Q. Jin, *Solid State Comm.* 148, 538 (2008).
8. F.C. Hsu, J.Y. Luo, K.W. Yeh, T.K. Chen, T.W. Huang, P.M. Wu, Y.C. Lee, Y.L. Huang, Y.Y. Chu, D.C. Yan, and M.K. Wu, *Proc. Natl. Acad. Sci. U.S.A.* 105, 14262 (2008).
9. C. Löhnert, T. Stürzer, M. Tegel, R. Frankovsky, G. Friederichs, and D. Johrendt, *Angew. Chem. Int. Ed.* 50, 9195 (2011).
10. N. Ni, J.M. Allred, B.C. Chan, and R.J. Cava, *Proc. Natl. Acad. Sci. USA* 108, E1019 (2011).
11. S. Kakiya, K. Kudo, Y. Nishikubo, K. Oku, E. Nishibori, H. Sawa, T. Yamamoto, T. Nozaka, and M. Nohara, *J. Phys. Soc. Jpn.* 80, 093704 (2011).
12. S.A. Sefat, *Curr. Op. Sol. St. Mat. Sci.* 17, 59–64 (2013).
13. T. Katase, S. Iimura, H. Hiramatsu, T. Kamiya, and H. Hosono, Phy. Rev. B. 85, 140516 (R) (2012)
14. T. Katase, H. Sato, H. Hiramatsu, T. Kamiya, and H. Hosono, Phy. Rev. B. 88, 140503 (R) (2013)
15. Y. Oner, and C. Boyraz, *Jour. Phy.: Cond. Matt.* 31, 155801 (2019).
16. C. Boyraz, A. Guler, and Y. Oner, *Jour. Supercon. Nov. Mag.* 31, 53 (2018).
17. A. Guler, M. Sertkol, and L. Saribaev, *IEEE Trans. Mag.* 51, 100504 (2015).
18. A. Iyo, S. Ishida, H. Fujihisa, Y. Gotoh, I. Hase, Y. Yoshida, H. Eisaki, and K. Kawashima, *J. Phys. Chem. Lett.* 10, 1018 (2019).
19. P.J. Hirschfeld, M.M. Korshunov, and I.I. Mazin, *Rep. Prog. Phys.* 74, 124508 (2011).

20. R. S. Dhaka, R. Jiang, S. Ran, S. L. Bud'ko, P. C. Canfield, B. N. Harmon, A. Kaminski, M. T. R. Valentí, and Y. Lee, Phys. Rev. B 89, 020511(R) (2014)
21. I.I. Mazin, M. Shimizu, N. Takemori, and H.O. Jeschke, *Phy. Rev. Lett.* 123, 267001 (2019).
22. J. Matsumoto, K. Hanzawa, M. Sasase, S. Haindl, T. Katase, H. Hiramatsu, and H. Hosono, *Phy. Rev. Mat.* 3, 103401 (2019).
23. H. Masatoshi, S. Iimura, K.M. Kojima, J.I. Yamaura, H. Hiraka, K. Ikeda, P. Miao, Y. Ishikawa, S. Torii, M. Miyazaki, I. Yamauchi, A. Koda, K. Ishii, M. Yoshida, J. Mizuki, R. Kadono, R. Kumai, T. Kamiyama, T. Otomo, Y. Murakami, S. Matsuishi, and H. Hosono, *Nat. Phy.* 10, 300 (2014).
24. S. Iimura, S. Matsuishi, H. Sato, T. Hanna, Y. Muraba, S.W. Kim, J.E. Kim, M. Takata, and H. Hosono, *Nat. Commun.* 3, 943 (2012).
25. C.H. Lee, A. Iyo, H. Eisaki, H. Kito, M.T.F. Diaz, T. Ito, K. Kihou, H. Matsuhata, M. Braden, and K. Yamada, *J. Phys. Soc. Jpn.* 77, 083704 (2008).
26. J. Zhao, Q. Huang, C. Cruz, S. Li, J.W. Lynn, Y. Chen, M.A. Green, G.F. Chen, G. Li, Z. Li, J.L. Luo, N.L. Wang, and P. Dai, *Nat. Mater.* 7, 953 (2008).
27. Y. Mizuguchi, Y. Hara, K. Deguchi, S. Tsuda, T. Yamaguchi, K. Takeda, H. Kotegawa, H. Tou, and Y. Takano, *Supercond. Sci. Technol.* 23, 054013 (2010).
28. K. Kuroki, H. Usui, S. Onari, R. Arita, and H. Aoki, *Phys. Rev. B.* 79, 224511 (2009).
29. H. Usui, and K. Kuroki, *Phys. Rev. B.* 84, 024505 (2011).
30. T. Saito, S. Onari, and H. Kontani, *Phys. Rev. B.* 82, 144510 (2010).
31. J. Zhao, Q. Huang, C. Cruz, S. Li, J.W. Lynn, Y. Chen, M.A. Green, G.F. Chen, G. Li, Z. Li, J.L. Luo, N.L. Wang, and P. Dai, *Nat. Mat.* 7, 953 (2008).
32. Y. Oner, C. Boyraz, and A. Güler, *Phy. C. Supcon. Its App.* 574, 1353665 (2020).
33. V. Grinenko, K. Kikoin, S.L. Drechsler, G. Fuchs, K. Nenkov, S. Wurmehl et al., *Phys. Rev. B.* 84, 134516 (2011).
34. W.A. Fietz, and W.W. Webb, *Phys. Rev.* 178, 657 (1969).
35. C.P. Bean, *Phys. Rev. Lett.* 8, 250 (1962).
36. V.D. Okunev, Z.A. Samoilenko, A. Szewczyk, R. Szymczak, H. Szymczak, P. Aleshkevych, J. Wieckowski, V.S. Khmelevskaya, and I.A. Antosh, *J. Phys.: Condens. Matt.* 22, 296001 (2010).
37. D.D. Hughes, *Philos. Mag.* 30, 293 (1974).
38. E.J. Kramer, *J. Appl. Phy.* 44, 1360 (1973).
39. A.M. Campbell, and J.E. Evetts, *Adv. Phys.* 21, 199–428 (1972).
40. M.R. Koblischka, A.J.J. Van Dalen, T. Higuchi, S.I. Yoo, and M. Murakami, *Phy. Rev. B.* 58, 2863–2867 (1998).
41. M. Eisterer, *Phys. Rev. B.* 77, 144524 (2008).
42. Y. Yeshurun, A.P. Malozemoff, F. Holtzberg, and T.R. Dinger, *Phys. Rev. B.* 38, 11828 (1988).
43. Y. Yeshurun, A.P. Malozemoff, T.K. Worthington, R.M. Yandrofski, L.K. Elbaum, F.H. Holtzberg, T.R. Dinger, and G.V. Chandrashekhar, *Cryogen.* 29, 258 (1989).
44. Y. Yeshurun, N. Bontemps, L. Burlachkov, and A. Kapitulnik, *Phys. Rev. B.* 49, 1548 (1994).
45. Y. Abulafia, A. Shaulov, Y. Wolfus, R. Prozorov, L. Burlachkov, Y. Yeshurun, D. Majer, E. Zeldov, H. W¨uhl, V. B. Geshkenbein, and V. M. Vinokur, Phys. Rev. Lett. 77, 1596 (1996)
46. G.M. Zhang, Y.H. Su, Z.Y. Lu, Z.Y. Weng, D.H. Lee, and T. Xiang, *EPL* 86, 37006 (2009).
47. S. Senoussi, M. Qussena, G. Collin, and I.A. Campbell, *Phys. Rev. B.* 37, 9792 (1988).
48. L.K. Elbaum, L. Civale, V.M. Vinokur, and F. Holtzberg, *Phys. Rev. Lett.* 69, 2280 (1992).
49. T. Higuchi, S.I. Yoo, and M. Murakami, *Phys. Rev. B.* 59, 1514 (1999).
50. M. V. Feigel'man, V. B. Geshkenbein, A. I. Larkin, and V. M. Vinokur, Phys. Rev. Lett. 63, 2303 (1989).
51. S. Sundar, S.S. Sugui Jr., E. Lovell, A. Vanstone, L.F. Cohen, D. Gong, R. Zhang, X. Lu, H. Luo, L. Ghivelder, and A.C.S. Appl, *Electron. Mater.* 1, 179 (2019).
52. Z. Devizorova, S. Mironov, and A. Buzdin, *Phys. Rev. Lett.* 122, 117002 (2019).
53. R. Micnas, J. Ranninger, and S. Robaszkiewicz, *Phys. Rev. B.* 36, 4051 (1987).
54. S. Kasahara, T. Shibauchi, K. Hashimoto, K. Ikada, S. Tonegawa, R. Okazaki, H. Shishido, H. Ikeda, H. Takeya, K. Hirata, T. Terashima, and Y. Matsuda, *Phys. Rev. B.* 81, 184519 (2010).
55. V.A. Gasparov, F.W. Fabris, D.L. Sun, C.T. Lin, and J. Wosnitza, *JETP Lett.* 93, 26 (2011).
56. A.H. Wilson, *Proc. R. Soc. Lond.* 167, 580 (1938).
57. L. Fang, H. Luo, P. Cheng, Z. Wang, Y. Jia, G. Mu, B. Shen, I. I. Mazin, L.Shan, C. Ren, and H. Hu. Wen, Phys. Rev. B. 80, 140508 (R) (2009)
58. Y. Oner, C. Boyraz, H. Hiramatsu, T. Katase, and H. Hosono, *Jour. Phy.: Con. Matt.* 32, 48 (2020).
59. S. Avci, O. Chmaissem, D.Y. Chung, S. Rosenkranz, E.A. Goremychkin, J.P. Castellan, I.S. Todorov, J.A. Schlueter, H. Claus, A. Daoud-Aladine, D.D. Khalyavin, M.G. Kanatzidis, and R. Osborn, *Phys. Rev. B.* 85, 184507 (2012).
60. K. Fischer, *Jour. Low Temp. Phys.* 17, 87 (1974).
61. N. Rivier, and M.J. Zuckermann, *Phys. Rev. Lett.* 13, 904 (1968).
62. E. Arushanov, G. Fuchs, S. Levcenko, S.L. Drechsler, B. Holzapfel, and L. Schultz, *Supercond. Sci. Technol.* 24, 105004 (2011).
63. Y. Oner, and S. Avci, *Jour. Elec. Mat.* 48, 2208 (2019).